

1  
2  
3  
4 **Phase Characterization of Cold Sector Southern Ocean Cloud Tops: Results**  
5 **from SOCRATES**

6 *Troy J. Zaremba<sup>1</sup>, Robert M. Rauber<sup>1</sup>, Greg M. McFarquhar<sup>2,3</sup>, Matthew Hayman<sup>4</sup>, Joseph A.*  
7 *Finlon<sup>5</sup>, and Daniel M. Stechman<sup>2,6</sup>*

8 <sup>1</sup>Department of Atmospheric Sciences, University of Illinois at Urbana-Champaign, Urbana,  
9 Illinois

10 <sup>2</sup>Cooperative Institute for Mesoscale Meteorological Studies, University of Oklahoma, Norman,  
11 Oklahoma

12 <sup>3</sup>School of Meteorology, University of Oklahoma, Norman, Oklahoma

13 <sup>4</sup>National Center for Atmospheric Research, Boulder, Colorado

14 <sup>5</sup>Department of Atmospheric Sciences, University of Washington, Seattle, Washington

15 <sup>6</sup>NOAA/OAR National Severe Storms Laboratory, Norman, Oklahoma

16  
17  
18  
19 Corresponding Author:  
20 Troy Zaremba  
21 University of Illinois at Urbana-Champaign  
22 4044 Natural History Building  
23 1301 W. Green St.  
24 Urbana, IL 61801  
25 815-245-0031  
26 tzaremb2@illinois.edu  
27

## KEY POINTS

- Airborne radar, lidar, and thermodynamic data are used to determine Southern Ocean cloud top phase as a function of cloud top temperature.
- Considering only clouds with subfreezing cloud top temperatures, the dominant phase at cloud top in 74.9% of clouds was liquid.
- Liquid-bearing cloud tops were even found at temperatures as cold as  $-30^{\circ}\text{C}$ .

## ABSTRACT

For a given cloud, whether the cloud top is predominately made up of ice crystals or supercooled liquid droplets plays a large role in the clouds overall radiative effects. This study uses collocated airborne radar, lidar, and thermodynamic data from twelve high-altitude flight legs during the Southern Ocean Clouds, Radiation, Aerosol Transport Experimental Study (SOCRATES) to characterize Southern Ocean (SO) cold sector cloud top phase (i.e., within 96 m of top) as a function of cloud top temperature (CTT). A training dataset was developed to create probabilistic phase classifications based on High Spectral Resolution Lidar data and Cloud Radar data. These classifications were then used to identify dominant cloud top phase. Case studies are presented illustrating examples of supercooled liquid water at cloud top at different CTT ranges over the SO ( $-3^{\circ}\text{C} < \text{CTTs} < -28^{\circ}\text{C}$ ). During SOCRATES, 67.4% of sampled cloud top had CTTs less than  $0^{\circ}\text{C}$ . Of the subfreezing cloud tops sampled, 91.7% had supercooled liquid water present in the top 96 m and 74.9% were classified entirely as liquid-bearing. Liquid-bearing cloud tops were found at CTTs as cold as  $-30^{\circ}\text{C}$ . Horizontal cloud extent was also determined as a function of median cloud top height.

## PLAIN LANGUAGE SUMMARY

Low-level clouds over the Southern Ocean have a large effect on the region's radiation budget. The radiation budget is strongly influenced by the phase (liquid or ice) of cloud tops, which is where most solar radiation is reflected, and most infrared radiation is radiated to space. For this reason, identifying the phase of cloud tops is important. In this study, airborne radar, lidar, and temperature data from twelve high-altitude flight legs during the Southern Ocean Clouds, Radiation, Aerosol Transport Experimental Study (SOCRATES) are used to characterize Southern Ocean cloud top phase as a function of cloud top temperature. The results show that liquid is the dominant phase present in clouds over the Southern Ocean, with liquid present at cloud top temperatures as cold as  $-30^{\circ}\text{C}$ .

## 1. Introduction

The Southern Ocean (SO) is characterized by a high frequency of extratropical cyclones (e.g. Simmonds & Keay, 2000; Hoskins & Hodges, 2005). While these storms are dominated by deep frontal cloud cover, their cold sectors are often characterized by subsidence aloft and low-level stratocumulus typical of a shallow surface-based well-mixed layer (e.g. Haynes et al., 2011). Climatologies over the region suggest that more than 80% of the SO is covered by low-level cloud cover at any given time regardless of season (e.g. Hu et al., 2010; Haynes et al., 2011; McCoy et al., 2014a,b). Huang et al. (2014) noted that most of these low-level clouds have cloud top temperatures (CTTs) between -20°C and 0°C.

Low-level SO clouds are a large source of uncertainty in global climate models (GCMs) and have a large effect on the region's radiation budget. GCMs have been shown to have large biases in top of atmosphere radiation fluxes and often underestimate the amount of reflected shortwave radiation over the region on the order of  $10 \text{ W m}^{-2}$  (e.g. Li et al., 2013; Kay et al., 2012; Bodas-Salcedo et al., 2014; D'Alessandro et al., 2019) as a result of low simulated cloud fraction and less supercooled liquid water (SLW) at cloud top, contrary to available observations over the region (e.g. Bodas-Salcedo et al., 2016; Kay et al., 2016). Several modeling studies have attempted to reduce GCM uncertainty in shortwave biases over the SO. Recent studies have shown that reflected shortwave radiation can be increased by changing the distribution of relative humidity used for depositional growth of ice crystals (e.g. Furtado et al., 2017; D'Alessandro et al., 2019) or by changing the phase of cloud water detrained from convection (Kay et al., 2016). These studies produced representations of SO clouds that made them more reflective, but shortwave biases have not been completely resolved using these changes in methodology and/or parameterization. Satellite retrievals over the SO also indicate a higher frequency of multilayer

83 mixed-phase clouds making them different from elsewhere in the world (e.g. Huang et al., 2014;  
84 McCoy et al., 2014b, 2015; Tan et al., 2016). The higher occurrence of multi-layer mixed phase  
85 clouds may also play a role in the overall shortwave radiation bias present in climate models with  
86 multi-layered clouds introducing another level of uncertainty.

87 The prevalence of SLW over the SO is supported by a limited number of recent in-situ studies.  
88 The HIPPER Pole to Pole Observations (HIPPO; Chubb et al., 2013) 2009 – 2011 field campaign  
89 flew two research flights over the SO and recorded the first in-situ microphysics observations south  
90 of Macquarie Island (54°S). SLW was observed in SO clouds at temperatures as low as -22°C  
91 (Chubb et al., 2013). Ahn et al. (2017) detailed in-situ observations from 20 flights made over the  
92 SO to the southwest of Tasmania during the southern hemisphere winter. Of the clouds sampled,  
93 36.7% were mixed phase, 1.8% were glaciated, and 61.5% were liquid. Huang et al. (2017)  
94 compared in situ measurements with A-train (e.g. L’Ecuyer & Jiang 2010; Ackerman et al., 2018)  
95 observations to confirm that patchy mixed-phase cloud cover present over the SO was  
96 predominately supercooled. Mace & Protat (2018a,b) analyzed data from the Clouds, Aerosols,  
97 Precipitation, Radiation, and atmospheric Composition Over the southeRn OceaN (CAPRICORN;  
98 Protat et al. 2017; Mace & Protat 2018a,b) voyage during the Southern Hemisphere spring of 2016  
99 and used thermodynamic phase partitioning to compare upward-pointing lidar observations with  
100 the satellite-based Cloud-Aerosol Lidar with Orthogonal Polarization (CALIOP; Winker et al.  
101 2009). Mace & Protat (2018a,b) found a greater occurrence of ice phase in subfreezing low level  
102 clouds than what was reported by CALIOP.

103 The common presence of SLW at cloud top is supported by other satellite studies over the SO.  
104 Hu et al. (2010) used CALIOP cloud phase measurements and found that more than 95% of low-  
105 level clouds (cloud top height lower than 2 km) with CTTs between -40°C and 0°C were liquid and

that the majority of supercooled clouds present were located within extratropical cyclone storm tracks. Huang et al. (2012a,b; 2015) showed a large occurrence of SLW over the SO with a large fraction of supercooled liquid cloud tops similar to that reported by Hu et al. (2010). Bodas-Salcedo et al. (2016) used a combination of A-train satellite observations and radiative transfer calculations to quantify the impact of cloud top phase on reflected solar radiation over the SO. They classified cloud top phase using three different methods and found supercooled cloud top occurrence ranging from 60-84%. Modeling showed that clouds with SLW at cloud top contributed between 27% and 38% of the total reflected solar radiation between 40°S and 70°S. Beyond these studies little work has been done to determine cloud top phase over the SO, especially from an airborne radar and lidar remote sensing perspective.

Understanding cloud properties over the SO is crucial as many uncertainties remain regarding their fine-scale structure and phase composition. From 15 January to 24 February 2018, the National Science Foundation (NSF)/National Center for Atmospheric Research (NCAR) Gulfstream-V (GV) High-performance Instrumented Platform for Environmental Research (HIAPER) aircraft flew over the SO during the SO Clouds, Radiation, Aerosol Transport Experimental Study (SOCRATES; McFarquhar et al. 2017) to make remote and in-situ measurements of the microphysical structure of boundary layer clouds. SOCRATES collected remote sensing and in-situ data that extends upon previous field campaigns over the SO. The addition of radar, lidar, and thermodynamic profiles collected during the campaign allows for more accurate quantification of cloud top phase (CTP).

The objective of this study is to quantify, using airborne lidar, W-band radar, and dropsonde measurements, the fraction of sampled cold sector cloud tops observed during SOCRATES dominated by SLW as a function of CTT. Phase identification is based on a lidar phase detection

scheme, developed herein, that can differentiate between regions of cloud top dominated by liquid or ice. The remainder of this paper is organized as follows. Section 2 details the flight strategy, data used, and methodology employed to process the radar, lidar, and dropsonde data. The lidar phase classification algorithm is described in Sec. 3, cloud top identification in Sec. 4, an overview of sampled cloud characteristics in Sec. 5, case studies illustrating SLW at cloud top at a range of CTTs in Sec 6, and CTP characteristics in Section 7. Sec. 8 considers potential phase characterization of cloud tops characterized by the phase identification algorithm as uncertain. Key findings are summarized in Sec. 9.

## **2. Data Overview**

This paper uses data collected by the HIAPER Cloud Radar (HCR), the HIAPER High Spectral Resolution Lidar (HSRL), and dropsonde data during twelve of the fifteen SOCRATES research flights that occurred in January and February 2018. These 12 flights were the only flights when thermodynamic, lidar, and radar data coexist. Dropsondes were not available on the other three flights.

The GV primarily sampled low-level boundary layer clouds in the cold sector of SO extratropical cyclones. Each SOCRATES research flight consisted of an initial high-altitude flight leg southbound at approximately 5.5 km above sea level (ASL) over the SO from Hobart, Tasmania (42.9°S, 147.5°E) to approximately 62°S. To sample clouds below the aircraft altitude during these initial legs, the HCR was pointed at nadir and the HSRL 4° off nadir (with the beam pointed normal to the aircraft flight direction) to avoid specular reflection from ice particles. Dropsondes were also periodically deployed (Fig. 1). Table 1 summarizes the times of the high-altitude flight legs analyzed in this paper and the number of dropsondes deployed during each leg.

### *2.1 HCR Data*

The HCR and its calibrations are described in Rauber et al. (2017). The HCR is a W-band Doppler radar mounted beneath the right wing of the GV that can detect ice particles, cloud droplets, and drizzle and has a  $0.7^\circ$  beamwidth. For SOCRATES, the HCR range resolution was 19.2 m, the along track resolution was 24 m at 1 km and 135 m at 5.5 km below the aircraft, and the temporal resolution was 10 Hz. HCR measurements of equivalent reflectivity factor (hereafter, reflectivity,  $Z_e$ ), and vertical Doppler radial velocity ( $V_r$ ) are used in this analysis (see Appendix B for a variable list). Precise quantitative estimates of  $Z_e$  were not required for this study, so no attempt to correct  $Z_e$  for attenuation was made.

The HCR data was quality controlled at NCAR. Range gates were first masked if the noise power exceeded the signal power. Then, if the HCR signal to noise ratio (SNR) was less than -10 dB, and the HCR normalized coherent power (NCP) was less than 0.1, range gates were masked as missing. Individual radar beams were then checked for isolated range gates that were only 1 or 2 gates in length. If isolated gates were surrounded by missing values, they too were masked as missing. Fig. 2a-b show NCP and SNR for RF02, and Fig. 2c shows  $Z_e$  (in dBZ<sub>e</sub>) after the NCAR thresholds were applied.

## 2.2 HSRL Data

The HSRL (HSRL; Razenkov et al, 2002; Eloranta et al., 2005; Eloranta et al., 2008; HIAPER HSRL; Albrecht et al., 2019; Schwartz et al., 2019) is a 532 nm wavelength, 300 mW lidar with a 7.5 m range resolution, and a temporal resolution of 2 Hz. The HSRL measures the backscatter optical power in separate combined (particle and molecular), molecular, and cross polarized channels to calculate the backscatter coefficient ( $\beta$ ) and linear depolarization ratio ( $\delta_p$ ) of the return signal from cloud and aerosol particles. The quantity  $\beta$  is a measure of how strongly the volume sampled scatters light back to the lidar at a  $180^\circ$  scattering angle. It is obtained through



the ratio of total combined (particle and molecular) backscatter to molecular backscatter and represents the linear sum of the backscatter cross section of each particle present in the sample volume. The quantity  $\delta_p$  measures the degree to which particles in a scattering volume modify the polarization state of incident light. The linear depolarization ratio is obtained using combined and cross-polarized returns and the ratio of total to molecular scattering. It is calculated under the assumption that the particles are randomly oriented and is an indicator of the asphericity of particles in a scattering volume. In this paper, these two lidar parameters ( $\beta$  and  $\delta_p$ ) will be used to discriminate between ice, liquid, and aerosol populations. In the case of  $\delta_p$ , the diluting effect of molecular scattering within a sampled volume has been removed. Individual lidar range gates were masked by NCAR prior to data release when  $\delta_p$  returns were unphysical (less than 0 or greater than 1) or if the photon counts in the combined high (parallel polarized) channel were below two photons because there was not high enough molecular SNR to calculate  $\delta_p$ .

### 2.3 NCAR Merged HCR/HSRL Dataset

After applying the HCR and HSRL threshold masks described above, NCAR interpolated the HCR and HSRL data to a uniform georeferenced grid of 2 Hz temporal and 19.2 m vertical resolution. First, the HCR data were averaged to 2 Hz to match the HSRL sampling rate. Then the closest HSRL range gate to each HCR range gate was used to resample the HSRL data to match the HCR range resolution. The HSRL did not observe the exact same cloud region as the HCR because it was pointed 4° off nadir to avoid specular reflection from ice crystals during high-altitude legs. The differences between the HSRL beam and the HCR beam for a flight altitude of 5.5 km was 70 m 1 km below the GV, 245 m 3.5 km below the GV (boundary layer cloud top at 2 km), and 385 m 5.5 km (the ocean surface) below the GV (Schwartz et al., 2019). The average width of a cloud top generating cell sampled over the SO was  $395 \pm 162$  m (Wang et al., 2020). If

cloud top height in the lower boundary layer was  $\sim 2$  km, for example, different parts of cloud top could be sampled simultaneously by the HCR and HSRL. These differences have no impact on the phase identification algorithm, since the HCR is only used to locate warm clouds with cloud top temperatures  $> 0^{\circ}\text{C}$ , and used to identify periods where the aircraft was flying through cloud that had temperatures  $< -10^{\circ}\text{C}$  (see Sec. 3.3).

The merged HCR/HSRL dataset consisted of vertical atmospheric columns that had along-track horizontal resolution of 75 to 110 m, depending on aircraft ground speed. Each column contained volume elements with 19.2 m vertical resolution. With the GV flying at approximately 5.5 km, a vertical column contained 286 volume elements, hereafter referred to as *elements*. The first 22 elements (422.4 m) sampled below the aircraft in each column were masked to eliminate near field effects of the aircraft. Elements within 100 m of the ocean surface were also masked to avoid contamination by the ocean surface. Fig. 3 summarizes the processing steps used to develop the phase classification algorithm, and the sections of the paper where each step is described.

#### 2.4 Dropsonde Data

Temperature from dropsonde curtains was incorporated into the HCR/HSRL merged dataset. The average vertical resolution of all dropsondes used in this analysis was 13.2 m, the average horizontal displacement between flight level and the surface was 8.4 km (See Table 1 for ranges from each research flight), the average distance between dropsondes launched was 174.3 km (See Table 1 for ranges from each research flight), and the accuracy of the dropsonde sensors was  $\pm 0.2^{\circ}\text{C}$  for temperature (UCAR, 2020). Dropsonde data were interpolated back to the closest great circle distance between the dropsonde position and the flight track (i.e. to the closest HCR/HSRL column) and then the height was matched to the closest column element in the merged HCR/HSRL

dataset. The dropsonde data were then interpolated using a linear interpolation over the entire high-altitude cross section to the center of all elements in the HCR/HSRL merged dataset.

### *2.5 Cloud liquid water measurements*

Measurements from a cloud droplet probe (CDP; Lance et al., 2010; Lance, 2012), Rosemount Icing Detector (RICE; Baumgardner & Rodi, 1989), and a 2D stereo probe (2D-S; Lawson et al., 2006) were used to determine if SLW was present while the GV was flying through cloud during high-altitude flight legs. The CDP measures the number concentrations of droplets between 2 and 50  $\mu\text{m}$ . Periods with CDP concentrations  $> 10 \text{ cm}^{-3}$  were identified as potential periods with SLW present (e.g. Hobbs and Rangno, 1998; Cober et al., 2001; Lance et al., 2010; Um et al., 2018; Finlon et al., 2019). The RICE was also used to identify when SLW was present based on voltage changes. Periods with a voltage change of at least  $2 \text{ mV s}^{-1}$  indicated the presence of SLW (Cober et al., 2001, McFarquhar et al., 2013; Wang et al., 2020). Cloud liquid water measurements were made at a rate of 1 Hz and were linearly interpolated to 2 Hz to assign liquid water measurements to each column. The 2D-S has an optical resolution of 10  $\mu\text{m}$  and imaged particle sizes spanning  $0.05 < D < 3.2 \text{ mm}$ . 2D-S images were subjectively analyzed in order to look for characteristics of drizzle droplets while the GV was flying through cloud during high-altitude flight legs.

### **3. Cloud Phase Identification**

CTP characterization herein is based on analysis of  $\delta_p$  and  $\beta$  in column elements within 96 m of cloud top. The methodology resembles the approach of past ground-based and spaceborne lidar analyses that use two-dimensional histograms to classify cloud phase (e.g. Hu, 2007; Hu et al., 2009; Thorsen et al., 2015; Silber et al., 2018). In these studies, cloud phase was classified along an entire radar or satellite time series dependent upon where data fell on a two-dimensional  $\delta_p$  versus  $\beta$  histogram. Several studies set arbitrary fixed boundaries between different regions of the

two-dimensional histogram to discriminate cloud phase (e.g. Shupe et al., 2007; Luke et al., 2010). Some, such as Silber et al. (2018), drew boundaries based on minimums between different phase population distribution peaks on their two-dimensional histograms.

In this paper, a novel approach to identify CTP based on the creation of a training dataset is introduced. The approach allows CTP to be classified based on where individual elements fall on a two-dimensional  $\delta_p$  versus  $\beta$  histogram relative to binned probability thresholds determined from the training dataset.

### *3.1 Clear Air Mask*

Cloud boundaries have been discriminated from their surrounding environment in numerous ground-based (e.g. Clothiaux et al., 2000; Illingworth et al., 2007; Feng et al., 2014; Shupe et al., 2016), spaceborne (e.g. Liu, 2004; Hart et al., 2005), and airborne studies (e.g. Spinhirne et al., 1982; Cambell et al., 2002; McGill et al., 2004; Wang et al., 2012; Klingebiel et al., 2015; Schwartz et al., 2019; Albrecht et al., 2019). To isolate cloudy elements, NCAR applied a clear air mask to the merged HCR/HSRL dataset to mask all HCR/HSRL elements between the lidar and the highest cloud top below the aircraft. Elements were masked as clear air if  $\beta < 10^{-4} \text{ m}^{-1} \text{ sr}^{-1}$  and HSRL molecular  $\text{SNR} < 1$ , or if the lidar data were previously masked because  $\delta_p$  returns were unphysical. No clear air masking was performed in columns where the aircraft was in cloud. After the clear air mask was applied, cloud tops were easily identified in the HSRL data because of the extreme signal attenuation that occurred beyond cloud top. The clear air mask was examined subjectively for each flight leg and the resulting cloud boundaries conformed well, with one exception. In the marine boundary layer (MBL, lowest 1 km over the SO), the clear air mask could not distinguish between cloud tops and clear air because the signal from aerosol (presumably larger deliquesced sea-salt haze droplets) exceeded the  $\beta$  and HSRL molecular SNR thresholds. Fig. 2a,b shows the

original  $Z_e$  and  $\beta$  as well as elements remaining after the clear air mask was applied (Fig. 2c). The procedure to separate aerosol from cloud required additional processing (see Sec. 3.4).

### 3.2 SOCRATES Two-Dimensional Lidar Histogram

Fig. 4 shows the two-dimensional histogram ( $\delta_p$  versus  $\beta$ ) after the clear air mask was applied from the twelve high-altitude SOCRATES flight legs regardless of aerosol presence, cloud presence, or depth beneath cloud top. Fig. 4 includes cloud elements that could be liquid, ice, or mixed-phase, elements affected by single or multiple scattering, and elements associated with aerosol in the MBL. The bin width for Fig. 4 was 0.01  $\delta_p$  and  $\beta$  of 0.1  $\text{m}^{-1} \text{sr}^{-1}$ . The histogram has three density clusters where specific populations (cloud dominated by liquid, cloud dominated by ice, and cloud-free aerosol) are likely concentrated based on past lidar studies (e.g. Silber et al. 2018) that examined cloud cover and subsequent phase at visible wavelengths.

### 3.3 Training Dataset

A training dataset was developed to separate cloud water, cloud ice, and aerosol based on radar, lidar, thermodynamic, and flight level measurements using the combined dataset for all columns from the 12 research flights using the following methodology:

To isolate elements composed entirely of cloud liquid water ( $L$ ), all columns where the clear air mask extended from the aircraft through the 0°C isotherm, *and* the noise threshold ( $\text{NCP} > 0.1$  or  $\text{SNR} > -10 \text{ dB}$ ) for  $Z_e$  was exceeded at altitudes somewhere below the altitude of the 0°C isotherm were isolated. Clouds in these columns had CTTs  $> 0^\circ\text{C}$  and therefore were composed only of liquid. The  $\delta_p$  versus  $\beta$  were recorded from each of the first five consecutive elements below the aircraft with  $\text{NCP} > 0.1$  or  $\text{SNR} > -10 \text{ dB}$  (measurable  $Z_e$  present). The data from these five elements from each of the columns satisfying the above criteria together made up the liquid portion of the training dataset. These data typically had low  $\delta_p$  and high  $\beta$  (Fig. 5a). The bin widths

for Fig. 5(a-c) were  $0.01 \delta_p$  and  $\beta$  of  $0.1 \text{ m}^{-1} \text{ sr}^{-1}$ . There were 26,142 elements included in the liquid component of the training dataset.

To isolate elements composed entirely of cloud ice ( $I$ ), columns were identified where the GV was flying through cloud, and measurable  $Z_e$  ( $\text{NCP} > 0.1$  or  $\text{SNR} > -10 \text{ dB}$ ) was present in unmasked lidar elements directly below the aircraft level. Any columns with SLW present at the aircraft level (CDP concentrations  $> 10 \text{ cm}^{-3}$ , or RICE voltage changes  $> 2 \text{ mV s}^{-1}$ , or 2D-S images characteristic of drizzle droplets exhibiting probable Poisson spots (Korolev 2007; McFarquhar et al., 2013)) were rejected. Elements in the remaining columns were required to have temperatures  $< -10^\circ\text{C}$  and  $Z_e > -10 \text{ dBZ}$ . The  $\delta_p$  and  $\beta$  data from the first five consecutive elements below the aircraft satisfying these criteria in each column were assumed to represent cloud ice and their values recorded. These elements made up the ice portion of the training dataset shown in Fig. 5b and typically had higher  $\delta_p$  and lower  $\beta$  compared to the liquid training data. There were 18,698 elements included in the ice portion of the training dataset.

To isolate elements with aerosol ( $A$ ) only, one-second forward facing flight imagery was visually analyzed to identify columns where the aircraft was far from any clouds and no clouds were present below the aircraft. The lidar  $\delta_p$  and  $\beta$  in unmasked elements were assumed to represent aerosol. As noted earlier, these unmasked elements occurred exclusively in the boundary layer in cloud free columns and were assumed to contain deliquesced haze droplets. These elements made up the aerosol portion of the training dataset shown in Fig. 5c and typically had low  $\delta_p$  and low  $\beta$ . Times used to create the aerosol portion of the training dataset are listed in Table 2. There were 293,340 elements in the aerosol portion of the training dataset making it much larger than the ice and liquid portions. If the boundary layer in a cloud free column was 1 km deep it would have contributed 52 elements to the aerosol portion of the training dataset.

### 3.4 Probability Assignment and Phase Classification

The training dataset was gridded into bins with column (i) increments of  $0.025 \delta_p$  and row (j) dimensions of  $0.25 \text{ m sr}^{-1} \beta$  (Fig. 5d-f), with each bin containing  $L_{(i,j)}$  (number of liquid elements in a given gridded bin),  $I_{(i,j)}$  (number of ice elements in a given gridded bin), and  $A_{(i,j)}$  (number of aerosol elements in a given gridded bin). Bins with  $L_{(i,j)} + I_{(i,j)} + A_{(i,j)} < 30$  were excluded. Remaining bins were normalized by the total number of elements identified as  $L$ ,  $I$ , and  $A$  respectively, to account for differences in size of  $L$ ,  $I$ , and  $A$  in the training dataset.

$$m_{L(i,j)} = \frac{L_{(i,j)}}{\sum_i \sum_j L_{(i,j)}} \quad m_{I(i,j)} = \frac{I_{(i,j)}}{\sum_i \sum_j I_{(i,j)}} \quad m_{A(i,j)} = \frac{A_{(i,j)}}{\sum_i \sum_j A_{(i,j)}}$$

Then, if  $\frac{m_{L(i,j)}}{m_{L(i,j)} + m_{I(i,j)} + m_{A(i,j)}} > 0.95$ , lidar elements within that bin were assumed to be dominated by liquid. Similarly, if  $\frac{m_{I(i,j)}}{m_{L(i,j)} + m_{I(i,j)} + m_{A(i,j)}} > 0.95$ , lidar elements were assumed to be dominated by ice, and if  $\frac{m_{A(i,j)}}{m_{L(i,j)} + m_{I(i,j)} + m_{A(i,j)}} > 0.95$ , lidar elements were assumed to be deliquesced aerosol. The term “dominated by” is used here to recognize that classification of an element as liquid does not imply that there was no ice whatsoever in the cloud element, or liquid in a cloud element classified as ice. The classification represents the dominant phase in that element based on the lidar measurements at visible wavelengths. Bins falling outside the training dataset, and bins where the 0.95 threshold for  $L$ ,  $I$ , or  $A$  was not met were classified as *uncertain*. Fig. 6 shows phase probability in each i, j bin (for  $L$ ,  $I$ , and  $A$ ) based on the training dataset and Fig. 7 shows the final phase classification when the 0.95 threshold was used. The sensitivity to the 0.95 threshold was tested on all of the lidar elements by increasing the threshold from 0.95 to 0.99. Increasing the threshold caused the total number of uncertain elements within the training dataset to increase by 11.0%. Fig. 2d shows an example from RF02 of assumed phase after classification.

After classification, an aerosol mask was then employed based on the aerosol classification. Remaining elements were assumed to be cloud, and made up of liquid, ice, and uncertain elements. Fig. 2e shows remaining cloud elements present from RF02 after the aerosol mask was applied.

#### **4. Cloud top identification**

During the twelve high-altitude flight legs, 153,478 columns were sampled, 64.2% of which had clouds present with cloud tops detectable below the aircraft, 7.1% where the aircraft was in cloud and cloud top could not be detected, and 1.4% where the cloud top could not be detected because it was in the near field 22 elements below the aircraft (see Appendix A). Columns where the GV was flying through cloud, or where cloud was present in the first 22 elements beneath the aircraft were excluded from further analysis because cloud top could not be detected. To isolate the cloud top region in columns with cloud below the aircraft, the first unmasked element below the aircraft and the four elements directly beneath it (representing the top 96 m of cloud), were considered cloud top (Fig. 2f). The temperature and phase of each cloud top element was recorded. Fig. 2f shows an example of final CTP identification from RF02.

Cloud top was identified in 103,702 atmospheric columns. 64.8% of cloud-containing columns had cloud with five consecutive elements (Fig. 8). Cloud depth was at least 96 m in these columns. In some cases, detected clouds were less than 96 m in depth, either due to complete attenuation of the lidar signal after cloud top penetration or due to the presence of thin veil clouds. Of the cloud containing columns, 35.2% had cloud top depths less than 96 m. Only 1-3 consecutive elements were present beneath the initial cloud top element in these cases. After cloud top identification, 88.9% of all cloud top elements sampled were found to be classified as either dominated by liquid or dominated by ice. Of all of the cloud top elements sampled, 11.2% were classified as uncertain. These elements were unidentifiable based on the training dataset and probability threshold noted



in the previous section. The potential phase characteristics of the uncertain elements are explored further in Sec. 8 using the HCR data.

## **5. Cloud Characteristics**

During SOCRATES, the GV primarily sampled broken cumulus, broken stratocumulus, or continuous widespread stratocumulus in the cold sectors of SO extratropical cyclones. Fig. 9 shows visible reflectance of clouds over the SO from the Himawari-8 satellite during research flights in which different cloud regimes were sampled. Fig. 9a for example, shows that the GV sampled broken stratocumulus present over the SO during RF02. During RF04, the GV sampled open cellular convection as well as deep frontal cloud cover (Fig 9B). During RF06, the GV primarily sampled clear air helping provide HSRL data needed to build the aerosol training dataset (Fig. 9C). The GV primarily sampled shallow, broken cumulus during RF07 (Fig. 9D). During RF13 (Fig. 9E), the GV sampled widespread nonprecipitating stratocumulus present over the SO.

To better define the characteristics of sampled clouds, horizontal cloud extent dimensions were analyzed for all of the high-altitude flight legs as a function of median cloud top height (Fig. 10). A horizontal cloud segment sampled in Fig. 10 was defined as a group of consecutive columns that contain HSRL detected cloud top. Columns were analyzed on a column by column basis. If consecutive columns contained cloud top that was separated by a height difference of less than 200 m, the new column was considered part of the same cloud segment. If there was a 200 m jump or greater in cloud top height between two consecutive columns, a new cloud segment was started. Using these definitions, 1999 cloud segments were sampled during the 12 high-altitude flight legs covering 9285 km of the SO of the 14372 km sampled. The 10<sup>th</sup> percentile of horizontal cloud extent ranged from ~80 to 110 m, 25<sup>th</sup> percentile ranged from ~100 m – 700 m, 50<sup>th</sup> percentile ranged from ~200 m -2 km, 75<sup>th</sup> percentile ranged from ~400 m – 80 km, and 90<sup>th</sup> percentile ranged

from ~1 km –110 km (Fig. 10). There were several time periods where widespread unbroken stratocumulus had cloud tops that varied less than 200 m and extended hundreds of km. In one case, almost 1000 km.

Most stratocumulus clouds had cloud tops that were  $< 2.5$  km. At the same time, low level broken cumulus clouds often were located in the same altitude range resulting in a wide range of horizontal cloud extents when median cloud top height was between 0.5 and 2 km. Low-level cumulus typically had small horizontal extents ( $< 1$  km) and were common, resulting in large segment counts at lower altitudes. Midlevel clouds were periodically sampled during various high-altitude flight legs but were typically deeper precipitating stratiform clouds that had larger horizontal cloud extents, evidenced by larger median cloud extents between 3-5 km.

## **6. Examples of CTP identification within different CTT ranges**

Fig. 11 shows an example of liquid cloud tops with  $10^{\circ}\text{C} < \text{CTT} < 6^{\circ}\text{C}$  during RF14. Data from these clouds contributed to the liquid training dataset. Precipitating clouds are present in two regions. Between these regions (22:37:10 – 22:37:30 UTC), cloud top was identified by lidar, but  $Z_e$  was below the HCR SNR and NCP thresholds. These regions were likely composed of thin clouds with small-enough droplets to be beneath the sensitivity of the HCR. Cloud top is identified by the HSRL with high  $\beta$  ( $> -10^{-4} \text{ m}^{-1} \text{ sr}^{-1}$ ) at cloud top and low  $\delta_p$  ( $< 0.1$ ). Fig. 12 shows an example of liquid cloud tops with  $-5^{\circ}\text{C} < \text{CTT} < -3^{\circ}\text{C}$  during RF02. Weak updrafts ( $1\text{-}2 \text{ m s}^{-1}$ ) were present near cloud top, with ice likely forming and precipitating from the supercooled liquid tops. Fig. 13 shows an example of supercooled liquid cloud tops with  $-12^{\circ}\text{C} < \text{CTT} < -9^{\circ}\text{C}$  from RF06. This case illustrates thin stratiform veil clouds that were beneath the sensitivity of the HCR but detectable by the HSRL. Cloud tops were classified as liquid. Forward facing flight level imagery shown at 00:56:00 and 00:58:00 confirm cloud presence (Fig. 11). Fig. 14 shows an example of

cloud tops detected with  $-18^{\circ}\text{C} < \text{CTT} < -8^{\circ}\text{C}$  from RF11. This case illustrates a deeper cloud system with ice production in the cloud and a definitive melting layer based on  $V_r$  measurements. Cloud depth and CTT varied substantially. Cloud tops in some regions were classified as liquid, while others were classified as uncertain. Uncertain elements in this case typically had low  $\beta$  ( $< 10^{-2} \text{ m}^{-1} \text{ sr}^{-1}$ ) and high  $\delta_p$  ( $> 0.1$ ) (not shown). Fig. 15 shows an example of liquid cloud top detected with  $-24^{\circ}\text{C} < \text{CTT} < -20^{\circ}\text{C}$ . The cloud was stratiform except near cloud top where weak updrafts on the order of  $1\text{--}2 \text{ m s}^{-1}$  were present. Ice likely formed near cloud top and precipitated based on  $V_r$  of  $\sim -1 \text{ m s}^{-1}$  above the melting level. Precipitation that formed in this case sublimated/evaporated before reaching the surface at the beginning of the period, but reached the surface later. Fig. 16 shows an example of liquid cloud top detected with  $-28^{\circ}\text{C} < \text{CTT} < -26^{\circ}\text{C}$  from RF03. Fall streaks in the  $Z_e$  field extend  $0.5 - 1 \text{ km}$  beneath the cloud top liquid layer at  $\sim 4.5 \text{ km}$ . Ice particles were apparently nucleated within the liquid layer near cloud top and precipitated from the base of the liquid layer. These data suggest that SLW at cloud top plays an important role in cold-sector SO clouds even at CTTs as cold as  $-30^{\circ}\text{C}$ . Liquid cloud top identified in these cases typically had high  $\beta$  ( $> 10^{-5} \text{ m}^{-1} \text{ sr}^{-1}$ ) and low  $\delta_p$  ( $< 0.1$ ) based on their distributions of  $\beta$  versus  $\delta_p$  (not shown).

## 7. Cloud top phase characteristics

Table 3 and Fig. 17 summarize the number of cloud-containing columns, cloud top elements present within those columns, and CTP classifications for each flight. The complete HCR/HSRL high-altitude cross section dataset used in this analysis is included in Appendix A. Appendix A contains cross sections of  $Z_e$ , lidar-identified cloud tops, CTP classification for each cloud top element, and the temperature field for each of the twelve high-altitude flight legs. Of all the cloud top elements combined, 87.5% were classified as liquid, 1.4% ice, and 11.2% uncertain (Table 3). The phase of elements as a function of depth within the cloud top region is presented in Fig. 18

and summarized in Table 4. The majority of cloud top elements were classified as liquid at depths up to 96 m beneath cloud top. Of all the cloud containing columns sampled, 78.5% were classified only as liquid and 0.5% of cloud-containing columns had cloud tops that were classified only as ice.

Fig. 19 shows CTP as a function of CTT and distance beneath cloud top. 67.4% of cloud columns sampled had CTTs that were less than 0°C. Of these columns, 91.7% contained at least one supercooled liquid element at cloud top and 74.9% had all cloud top elements classified as liquid. Element phase as a function of CTT is quantified in Table 5. Fig. 19 shows liquid cloud top elements present at CTTs as low as -30°C. 5.6% of cloud top columns sampled had CTTs between -30 °C and -20 °C. Within those columns, 50.4% of elements were classified as liquid and 46.4% as uncertain. Most cloud top elements classified as uncertain were detected at CTTs < -20°C. Of all the columns sampled, 61.8% had CTTs between -20°C and 0°C. Within these columns, 88.7% of the cloud top elements were classified as liquid, 1.5% ice, and 7.7% uncertain. A majority of sub-freezing cloud cover over the SO observed during SOCRATES had SLW present at all CTTs sampled, consistent with satellite observations over the region in previous studies (e.g. Hu et al., 2010).

## **8. Further Analysis of the Uncertain Phase**

Fig. 20 shows a breakdown of uncertain elements when reflectivity was above the noise threshold for all twelve high-altitude cross sections to show how  $\beta$  versus  $\delta_p$  distributions varied over 5°C temperature intervals from -30°C to 0°C. Flights over higher-altitude clouds, such as RF03, RF04, RF07, and RF11, had more cloud top elements classified as uncertain than those sampling only boundary layer clouds (e.g. RF02, RF12, and RF14) (see Appendix A). For example, many cloud top elements classified as uncertain during RF03 typically had CTTs < -

20°C. Typical  $\beta$  values in uncertain cloud top elements during RF03 were  $< 10^{-6} \text{ m}^{-1} \text{ sr}^{-1}$  with larger  $\delta_p$  ( $> 0.2$ ). At colder CTTs ( $< -20^\circ\text{C}$ ) uncertain elements typically had low  $\beta$  ( $< 10^{-5} \text{ m}^{-1} \text{ sr}^{-1}$ ) and higher  $\delta_p$  ( $> 0.2$ ) characteristic of ice (Fig. 20a,b). The infrequent occurrence of these elements with low  $\beta$  and high  $\delta_p$  led them to not be included in the training dataset. Note that at these temperatures, a small number of elements had high  $\beta$  ( $> 10^{-3} \text{ m}^{-1} \text{ sr}^{-1}$ ) and low  $\delta_p$  ( $< 0.1$ ), characteristic of liquid. At temperatures between  $-20^\circ\text{C}$  and  $-10^\circ\text{C}$ , a transition occurs with the distribution of uncertain elements shifting from higher  $\delta_p$  (mostly  $> 0.2$ , Fig. 20c) to progressively lower  $\delta_p$  (mostly  $< 0.2$ , Fig. 20d). These elements are likely mixed phase because of the relatively low  $\beta$  ( $< 10^{-4} \text{ m}^{-1} \text{ sr}^{-1}$ ), and progressively more dominated by liquid at higher temperatures. Here, as with Figs. 20a,b, elements with high  $\beta$  ( $> 10^{-3} \text{ m}^{-1} \text{ sr}^{-1}$ ) and low  $\delta_p$  ( $< 0.1$ ) were present, characteristic of liquid (Fig. 20c,d). At still higher temperatures ( $> -10^\circ\text{C}$ ) uncertain elements either had very low  $\beta$  and low  $\delta_p$  ( $< 0.1$ ), or had high  $\beta$  and low  $\delta_p$  ( $< 0.1$ ), largely surrounding the liquid training dataset. The data in total suggest that most uncertain cloud top elements at temperatures  $< -15^\circ\text{C}$  were mixed phase or ice phase, while those at temperatures  $> -15^\circ\text{C}$  were liquid phase.

## 9. Conclusions

This study used airborne remote sensing observations to determine and statistically represent cloud top phase (CTP) of cold sector clouds over the Southern Ocean (SO). The occurrence of supercooled liquid water (SLW) is especially important to quantify given its relevance to enhanced shortwave radiation reflectance. The main question addressed by this study is what percentage of cloud cover sampled during the Southern Ocean Clouds, Radiation, Aerosol Transport Experimental Study (SOCRATES) had SLW at cloud top as a function of cloud top temperature (CTT). A training dataset was developed for aerosol, cloud liquid, and cloud ice to create probabilistic phase classifications based on High Spectral Resolution Lidar (HSRL) data. These

classifications were used to differentiate between aerosol and cloud in the lower boundary layer, identify cloud top, and characterize CTP. Case studies were also presented illustrating examples of SLW at cloud top at different ranges of CTTs ( $-3^{\circ}\text{C} < \text{CTTs} < -28^{\circ}\text{C}$ ).

The key findings from this analysis of SOCRATES data are:

- 1) Of all cloud top elements sampled in the top 96 m of cloud top, 87.5% were classified as liquid, 1.4% ice, and 11.2% were uncertain (meaning they fell outside of the training dataset).
- 2) Of all the clouds sampled, 67.4% had cloud tops that were subfreezing. Considering only these clouds, 91.7% had at least one SLW element present at cloud top and 74.9% were classified entirely as liquid
- 3) For cloud tops between  $-20^{\circ}\text{C}$  and  $0^{\circ}\text{C}$ , 88.7% of the cloud top elements were classified as liquid, 1.5% ice, and 7.7% were uncertain.
- 4) For cloud tops colder than  $-20^{\circ}\text{C}$ , 50.4% of cloud top elements were classified as liquid, 2.9% ice, and 46.6% uncertain. A subsequent analysis of uncertain cloud top elements provided evidence that they were either mixed or ice phase at these temperatures.
- 5) Liquid-bearing cloud tops were found even at temperatures as cold as  $-30^{\circ}\text{C}$ .

SOCRATES provided new insight into SO boundary layer cloud properties through the use of airborne cloud radar, lidar, and thermodynamic observations. During SOCRATES, clouds most frequently had liquid-bearing cloud tops. Wang et al. (2020) analyzed in situ measurements of cloud top generating cells during the SOCRATES field campaign and found that all cloud top generating cells sampled had SLW at cloud top even at CTTs as cold as  $-33^{\circ}\text{C}$ . The ubiquitous presence of SLW at cloud top found in in-situ data from Wang et al. (2020) is consistent with the remote sensing results herein. Optically thick clouds fully attenuate the HSRL signal limiting

phase retrievals beneath cloud top on the high-altitude flight legs, but the retrieval algorithm developed herein allowed for identification of cloud top phase. More theoretical, observational, and modeling work needs to be done to better understand processes that maintain and sustain SLW at cloud top over the SO region.

## **Appendix A: HCR/HSRL high-altitude cross section dataset**

Figs. A1, A2, and A3 summarize each high-altitude flight leg sampled during SOCRATES with coincident lidar, radar and thermodynamic data. Figs. A1, A2, and A3 depict cross sections of  $Z_e$ , lidar-identified cloud tops, CTP classification for each cloud top element present, and the temperature field for each of the twelve high-altitude flight legs. Note that many clouds detected by the HSRL were not detected by the HCR. Columns where cloud is present, not present, where the GV is flying through cloud, or has near field effects are denoted by the lower bar on each high-altitude cross section. The phase of the first five elements detected at cloud top in each column are included in the top bar above each high-altitude cross section. If five elements were not present at cloud top due to thin veil cloud or attenuation, only 1-3 phase classified elements were present beneath cloud top.

RF02, RF12, RF14, and RF15 were all boundary layer cloud cases that sampled mixed-phase stratocumulus and cumulus clouds. RF03, RF04, RF10, and RF11 sampled deeper cloud cover over the SO whose tops were often above the GV flight level. RF05 and RF06 predominately sampled MBL aerosol. RF13 sampled low-level stratocumulus beneath the sensitivity of the HCR while RF07 sampled a non-precipitating cumulus field.

## **Appendix B: List of variables and their descriptions**

$A$	Aerosol elements in training dataset
$I$	Ice elements in training dataset
$L$	Liquid elements in training dataset
$m_A(i, j)$	Normalized number of aerosol elements in a gridded bin (row $i$ and column $j$ )

519	$m_I(i, j)$	Normalized number of ice elements in a gridded bin (row i and column j)
520	$m_L(i, j)$	Normalized number of liquid elements in a gridded bin (row i and column j)
521	NCP	Normalized Coherent Power
522	$A_{(i,j)}$	Number of aerosol elements in a gridded bin (row i and column j)
523	$I_{(i,j)}$	Number of ice elements in a gridded bin (row i and column j)
524	$L_{(i,j)}$	Number of liquid elements in a gridded bin (row i and column j)
525	SNR	Signal to noise ratio
526	$V_r$	Doppler radial velocity
527	$Z_e$	Equivalent radar reflectivity factor
528	$\beta$	Aerosol backscatter coefficient
529	$\delta_p$	Particle linear depolarization ratio
530		



## References

- Ackerman, S. A., Platnick, S., Bhartia, P. K., Duncan, B., L'Ecuyer, T., Heidinger A., Skofronick-Jackson, G., Leob, N., Schmit, T., & Smith, N. (2018). Satellites See the World's Atmosphere. *Meteor. Monogr.* 59, 4.1-4.53. <https://doi.org/10.1175/AMSMONOGRAPHIS-D-18-0009.1>
- Ahn, E., Huang, Y., Chubb, T. H., Baumgardner, D., Isaac, P., de Hoog, M., Siems, S., & Manton, M. (2017). In Situ Observations of Wintertime low-altitude clouds over the Southern Ocean. *Q. J. R. Meteorol. Soc.*, 143, 1381–1394. [doi.org/10.1002/qj.3011](https://doi.org/10.1002/qj.3011)
- Albrecht, B., Ghate, V., Mohrmann, J., Wood, R., Zudema, P., Bretherton, C., Schwartz, C., Eloranta, E., Glienke, S., Donaher, S., Sarkar, M., McGibbon, J., Nugent, A. D., Shaw, R. A., Fugal, J., Minnis, P., Paliknoda, R., Lussier, L., Jensen, J., Vivekanandan, J., Ellis, S., Tsai, P., Rilling, R., Haggerty, J., Campos, T., Stell, M., Reeves, M., Beaton, S., Allison, J., Stossmeister, G., Hall, S., & Schmidt, S. (2019). Cloud System Evolution in the Trades (CSET): Following the evolution of boundary layer cloud systems with the NSF–NCAR GV. *Bull. Amer. Meteor. Soc.*, 100, 93–121. <https://doi.org/10.1175/BAMS-D-17-0180.1>.
- Baumgardner, D., & Rodi, A. (1989). Laboratory and wind tunnel evaluations of the Rosemount icing detector. *J. Atmos. Oceanic Technol.*, 6 (6), 971–979. [doi.org/10.1175/1520-0426\(1989\)006<0971:LAWTEO>2.0.CO;2](https://doi.org/10.1175/1520-0426(1989)006<0971:LAWTEO>2.0.CO;2)
- Bodas-Salcedo, A., Hill, P. G., Furtado, K., Williams, K. D., Field, P. R., Manners, J. C., Hyder, P., & Kato, S. (2016). Large contribution of supercooled liquid clouds to the solar radiation budget of the Southern Ocean, *J. Clim.*, 29(11), 4213–4228. [doi.org/10.1175/JCLI-D-15-0564.1](https://doi.org/10.1175/JCLI-D-15-0564.1)

554 Bodas-Salcedo, A., Williams, K. D., Ringer, M. A., Beau, I., Cole, J., Dufresne, J. L., Koshiro,  
 555 T., Stevens, B., Wang, Z., & Yokohata, T. (2014). Origins of the solar radiation biases  
 556 over the Southern Ocean in CFMIP2 models. *J. Clim*, 27(1), f– 56. doi.org/10.1175/JCLI-  
 557 D-13-00169.1

558 Campbell, J. R., Hlavka, D. L., Welton, E. J., Flynn, C. J., Turner, D. D., Spinhirne, J. D., Scott,  
 559 V. S., & Hwang, I. H. (2002). Full-time, eye-safe cloud and aerosol lidar observations at  
 560 Atmospheric Radiation Measurement Program sites: Instruments and data processing. *J.*  
 561 *Atmos. Oceanic Technol.*, 19, 431–442. https://doi.org/10.1175/1520-  
 562 0426(2002)019,0431:FTESCA.2.0.CO;2.

563 Chubb, T. H., Jensen, J. B., Siems, S. T., & Manton M. J. (2013). In situ observations of  
 564 supercooled liquid clouds over the Southern Ocean during the HIAPER pole-to-pole  
 565 observation campaigns. *Geophys. Res. Lett.*, 40, 5280–5285. doi.org/10.1002/grl.50986

566 Clothiaux, E. E., Ackerman, T. P., Mace, G. G., Moran, K. P., Marchand, R. T., Miller, M. A., &  
 567 Martner, B. E. (2000). Objective determination of cloud heights and radar reflectivities  
 568 using a combination of active remote sensors at the ARM CART sites. *J. Appl. Meteor.*,  
 569 39, 645–665. https://doi.org/10.1175/1520-0450(2000) 039,0645:ODOCHA.2.0.CO;2.

570 Cober, S. G., Isaac, G. A., Korolev, A. V., & Strapp, J. W. (2001), Assessing cloud-phase  
 571 conditions, *J. Appl. Meteorol.*, 40(11), 1967-1983. doi.org/10.1175/1520-  
 572 0450(2001)040<1967:ACPC>2.0.CO;2

573 D'Alessandro, J. J., Diao, M., Wu, C., Liu, X., Jensen, J. B., & Stephens, B. B. (2019). Cloud  
 574 phase and relative humidity distributions over the Southern Ocean in Austral summer  
 575 based on in situ observations and CAM5 simulations. *J. Clim*, 32(10), 2781–2805.  
 576 doi.org/10.1175/JCLI-D-18-0232.s1

577 Eloranta, E. W., Razenkov, I. A., Hedrick, J., & Garcia, J. P. (2008). The design and construction  
 578 of an airborne high spectral resolution lidar. *Proc. 2008 IEEE Aerospace Conf.*, Big Sky,  
 579 MT, IEEE, 6 pp., <https://doi.org/10.1109/AERO.2008.4526390>.  
 580 Eloranta, E., (2005). High spectral resolution lidar. *Lidar: Range-Resolved Optical Remote*  
 581 *Sensing of the Atmosphere*, C. Weitkamp, Ed., Springer Series in Optical Sciences,  
 582 Springer-Verlag, 143–163.  
 585 Feng, Z., McFarlane, S. A., Schumacher, C., Ellis, S., Comstock, J., & Bharadwaj, N. (2014).  
 586 Constructing a merged cloud–precipitation radar dataset for tropical convective clouds  
 587 during the DYNAMO/AMIE experiment at Addu Atoll. *J. Atmos. Oceanic Technol.*, 31,  
 588 1021–1042, <https://doi.org/10.1175/JTECH-D-13-00132.1>.  
 589 Finlon, J. A., McFarquhar, G. M., Nesbitt, S. W., Rauber, R. M., Morrison, H., Wu, W., &  
 590 Zhang, P. (2019). A novel approach for characterizing the variability in mass–dimension  
 591 relationships: Results from MC3E. *Atmos. Chem. Physics*, 19(6), 3621–3643.  
 592 [doi.org/10.5194/acp-19-3621-2019](https://doi.org/10.5194/acp-19-3621-2019)  
 593 Furtado, K., & Field P. (2017). The role of ice microphysics parameterizations in determining  
 594 the prevalence of supercooled liquid water in high-resolution simulations of a Southern  
 595 Ocean midlatitude cyclone. *J. Atmos. Sci.*, 75, 2001–2021. [doi.org/10.1175/JAS-D-16-](https://doi.org/10.1175/JAS-D-16-0165.1)  
 596 [0165.1](https://doi.org/10.1175/JAS-D-16-0165.1)  
 597 Hart, W. D., Spinhirne, J. D., Palm, S. P., & Hlavka, D. L. (2005). Height distribution between  
 598 cloud and aerosol layers from the GLAS spaceborne lidar in the Indian Ocean region.  
 599 *Geophys. Res. Lett.*. <https://doi.org/10.1029/2005GL023671>

600 Haynes, J. M., Jakob, C., Rossow, W. B., Tselioudis, G., & Brown, J. (2011). Major  
 601 characteristics of Southern Ocean cloud regimes and their effects on the energy budget. *J.*  
 602 *Clim.*, 24(19), 5061-5080. doi.org/10.1175/2011JCLI4052.1  
 603 Hobbs, P. V., & Rangno, A. L. (1998). Microstructures of low and middle-level clouds over the  
 604 Beaufort Sea. *Q. J. R. Meteorol. Soc.*, 124(550), 2035–2071.  
 605 doi.org/10.1002/qj.49712455012  
 606 Hoskins, B. J., & Hodges, K. L. (2005). A New Perspective on Southern Hemisphere Storm  
 607 Tracks. *J. Clim.*, 18(20), 4108-4129. doi.org/10.1175/JCLI3570.1  
 608 Hu, Y. (2007). Depolarization ratio-effective lidar ratio relation: Theoretical basis for space lidar  
 609 cloud phase discrimination. *Geophys. Res. Lett.*, 34, L11812.  
 610 doi.org/10.1029/2007GL029584  
 611 Hu, Y., Rodier, S., Xu, K., Sun, W., Huang, J., Lin, B., Zhai, P., & Josset, D. (2010),  
 612 Occurrence, liquid water content, and fraction of supercooled water clouds from  
 613 combined CALIOP/IIR/MODIS measurements. *J. Geophys. Res. Atmos.*, 115, D00H34.  
 614 doi.org/10.1029/2009JD012384  
 615 Hu, Y., Winker, D., Vaughan, M., Lin, B., Omar, A., Trepte, C., Flittner, D., Yang, P., Nasiri, S.  
 616 L., Baum, B., Holz, R., Sun, W., Liu, Z., Wang, Z., Young, S., Stamnes, K., Huang, J.,  
 617 & Kuehn, R. (2009). CALIPSO/CALIOP cloud phase discrimination algorithm. *J. Atmos.*  
 618 *Oceanic Technol.*, 26(11), 2293–2309. doi.org/10.1175/2009JTECHA1280.1  
 619 Huang, Y., Protat, A., Siems, S. T., & Manton, M. J. (2015). A-Train observations of maritime  
 620 midlatitude storm-track cloud systems: Comparing the Southern Ocean against the North  
 621 Atlantic. *J. Clim.*, 28(5), 1920–1939. doi.org/10.1175/JCLI-D-14- 00169.1

622 Huang, Y., Siems, S. T., Manton, M. J., & Thompson, G. (2014). An evaluation of WRF  
623 simulations of clouds over the Southern Ocean with A-train observations. *Mon. Wea.*  
624 *Rev.*, 142, 647–667. doi.org/10.1175/MWR-D-13-00128.1

625 Huang, Y., Siems, S. T., Manton, M. J., Hande, L. B., & Haynes, J. M. (2012a). The structure of  
626 low-altitude clouds over the Southern Ocean as seen by CloudSat. *J. Clim.*, 25(7), 2535–  
627 2546. doi.org/10.1175/JCLI-D-11-00131.1

628 Huang, Y., Siems, S. T., Manton, M. J., Protat, A., & J. Delanoë, J. (2012b). A study on the low-  
629 altitude clouds over the Southern Ocean using the DARDAR-MASK. *J. Geophys. Res.*  
630 *Atmos.*, 117, D18204. doi.org/10.1029/2012JD017800

631 Huang, Y., Chubb, T., Baumgardner, D., deHoog, M., Siems, S. T., & Manton M. J. (2017).  
632 Evidence for secondary ice production in Southern Ocean open Cellular Convection. *Q.*  
633 *J. R. Meteorol. Soc.*, 143, 1685-1703. doi.org/10.1002/qj.3041

634 Illingworth, A. J., Hogan, R. J., O'Connor, E. J., Bouniol, D., Brooks, M. E., Delanoë, J.,  
635 Donovan, D. P., Eastment, J. D., Gaussiat, N., Goddard, J. W. F., Haeffelin, M., Baltink,  
636 H., Krasnov, O. A., Pelon, J., Piriou, J. -M., Protat, A., Russchenberg, H. W. J., Seifert,  
637 A., Tompkins, A. M., van Zadelhoff, G. -J., Vinit, V., Wilson, D. R., & Wrench, C. L.  
638 (2007). Cloudnet: Continuous evaluation of cloud profiles in seven operational models  
639 using ground-based observations. *Bull. Amer. Meteor. Soc.*, 88, 883–898.  
640 <https://doi.org/10.1175/BAMS-88-6-883>.

641 Kay, J. E., Hillman, B. R., Klein, S. A., Zhang, Y., Medeiros, B., Pincus, R., Gettelman, A.,  
642 Eaton, B., Boyle, J., Marchand, R., & Ackerman, T. P. (2012). Exposing global cloud  
643 biases in the Community Atmosphere Model (CAM) using satellite observations and

their corresponding instrument simulators. *J. Clim.*, 25, 5190–5207.  
<https://doi.org/10.1175/JCLI-D-11-00469.1>

Kay, J. E., Wall, C., Yettella, V., Medeiros, B., Hannay, C., Caldwell, P., & Bitz, C. (2016). Global climate impacts of fixing the Southern Ocean shortwave radiation bias in the Community Earth System Model (CESM). *J. Clim.*, 29, 4617–4636.  
[doi.org/10.1175/JCLI-D-15-0358.1](https://doi.org/10.1175/JCLI-D-15-0358.1)

Klingebiel, M., de Lozar, A., Molleker, S., Weigel, R., Roth, A., Schmidt, L., Meyer, J., Ehrlich, A., Neuber, R., Wendisch, & M., Borrmann, S. (2015). Arctic low-level boundary layer clouds: In situ measurements and simulations of mono- and bimodal supercooled droplet size distributions at the top layer of the liquid phase clouds. *Atmos. Chem. Phys.*, 15, 617–631. <https://doi.org/10.5194/acp-15-617-2015>

Korolev, A. V. (2007). Reconstruction of the sizes of spherical particles from their shadow images. Part I: Theoretical considerations. *J. Atmos. Oceanic Technol.*, 24, 376–389.  
[doi.org/10.1175/JTECH1980.1](https://doi.org/10.1175/JTECH1980.1)

Lance, S. (2012). Coincidence Errors in a Cloud Droplet Probe (CDP) and a Cloud and Aerosol Spectrometer (CAS), and the Improved Performance of a Modified CDP. *J. Atmos. Oceanic Technol.*, 29(10), 1532–1541. [doi.org/10.1175/JTECH-D-11-00208.1](https://doi.org/10.1175/JTECH-D-11-00208.1)

Lance, S., Brock, C. A., Rogers, D., & Gordon, J. A. (2010). Water droplet calibration of the cloud droplet probe (CDP) and in-flight performance in liquid, ice and mixed-phase clouds during ARCPAC. *Atmos. Meas. Tech.*, 3, 1683–1706. [doi.org/10.5194/amt-3-1683-2010](https://doi.org/10.5194/amt-3-1683-2010)

Lawson, P., O'Connor, D., Zmarzly, P., Weaver, K., Baker, B. A., Mo, Q., & Jonsson, H. (2006). The 2DS (stereo) probe: Design and preliminary tests of a new airborne, high speed,

667 high-resolution particle imaging probe. *J. Atmos. Oceanic Technol.*, 23, 1462–1471.  
 668 doi.org/10.1175/JTECH1927.1  
 669 L’Ecuyer, T. S., & Jiang J. H. (2010). Touring the atmosphere aboard the A-Train. *Phys Today*,  
 670 63, 36-41. <https://doi.org/10.1063/1.3463626>  
 671 Li, J., Waliser, D. E., Stephens, G., Lee, S., L’Ecuyer, T., Kato, S., Loeb, N., & Ma, H.-Y.  
 672 (2013). Characterizing and understanding radiation budget biases in CMIP3/CMIP5  
 673 GCMs, contemporary GCM, and reanalysis. *J. Geophys. Res. Atmos.*, 118, 8166–8184,  
 674 <https://doi.org/10.1002/jgrd.50378>.  
 679 Liu, Z., Vaughan, M. A., Winker, D. M., C. A. Hostetler, C. A., Poole, L. R., Hlavka, D., Hart,  
 680 W., & McGill, M. (2004). Use of probability distribution functions for discriminating  
 681 between cloud and aerosol in lidar backscatter data. *J. Geophys. Res. Atmos.*, 109,  
 682 D15202. <https://doi.org/10.1029/2004JD004732>.  
 683 Luke, E. P., Kollias, P., & Shupe, M. D. (2010). Detection of Supercooled Liquid in Mixed-  
 684 Phase Clouds using Radar Doppler Spectra. *J. Geophys. Res. Atmos.* 115, D19201.  
 685 doi.org/10.1029/2009JD012884  
 686 Mace, G. G., & Protat, A. (2018a), Clouds over the Southern Ocean as observed from the RV  
 687 Investigator during CAPRICORN, Part 1: Cloud occurrence and phase partitioning. *J.*  
 688 *Appl. Meteorol.*, 57. doi.org/10.1175/JAMC-D-17-0194.1  
 689 Mace, G. G., & Protat, A. (2018b), Clouds over the Southern Ocean as observed from the RV  
 690 Investigator during CAPRICORN, Part 2: The properties of non-precipitating  
 691 stratocumulus. *J. Appl. Meteorol.*, 57. doi.org/10.1175/JAMC-D-17-0195.1

692 McCoy, D. T., Hartmann, D. L., Zelinka, M. D., Ceppi, P., & Grosvenor, D. P. (2015). Mixed-  
693 phase cloud physics and Southern Ocean cloud feedback in climate models. *J. Geophys.*  
694 *Res. Atmos.*, 120, 9539–9554. doi.org/10.1002/2015JD023603.

695 McCoy, D. T., Hartmann, D. L., & Grosvenor D. P. (2014b). Observed Southern Ocean cloud  
696 properties and shortwave reflection, Part II: Phase changes and low cloud feedback. *J.*  
697 *Clim.*, 27(23), 8858– 8868. doi.org/10.1175/JCLI-D-14-00288.1

698 McCoy, D. T., Hartmann, D. L., & Grosvenor, D. P. (2014a). Observed Southern Ocean Cloud  
699 Properties and Shortwave Reflection. Part I Calculation of SW Flux from Observed  
700 Cloud Properties. *J. Clim.*, 27(22) 8836 – 8857. doi.org/10.1175/JCLI-D-14-00287.1

701 McFarquhar, G. M., Um, J., & Jackson, R. (2013). Small cloud particle shapes in mixed-phase  
702 clouds. *J. Appl. Meteor. Climatol.*, 52, 1277–1293. doi.org/10.1175/JAMC-D-12-0114.1.

703 McFarquhar, G. M., Marchand, R., Wood, R., Bretherton, C., Protat, A., Quinn, P., Siems, S.,  
704 Jakob, C., & Weller, B. (2017). The Southern Ocean Clouds, Radiation, Aerosol  
705 Transport Experimental Study. <https://www.osti.gov/servlets/purl/1240753>. Accessed 17  
706 September 2020.

707 McFarquhar, G. M., Baumgardner, D., Bansemer, A., Abel, S. J., Crosier, J., French, J.,  
708 Rosenberg, P., Korolev, A., Schwarzenboeck, A., Leroy, D., Um, J., Wu, W.,  
709 Heymsfield, A. J., Twohy, C., Detwiler, A., Field, P., Neumann, A., Cotton, R., Axisa,  
710 D., & Dong, J. (2017). Processing of ice cloud in situ data collected by bulk water,  
711 scattering, and imaging probes: Fundamentals, uncertainties, and efforts toward  
712 consistency. *Meteor. Monogr* , 58, 11.1–11.33.  
713 <https://doi.org/10.1175/AMSMONOGRAPHS-D-16-0007.1>.



714 McGill, M., Li, L., Hart, W. D., Heymsfield, G. M., Hlavka, D. L., Racette, P. E., Tian, L.,  
 715 Vaughan, M. A., & Winker, D. M. (2004). Combined lidar-radar remote sensing: Initial  
 716 results from CRYSTAL-FACE. *J. Geophys. Res. Atmos.*, 109, D07203.  
 717 doi.org/10.1029/2003JD004030.

742 Protat, A., Schulz, E., Rikus, L., Sun, Z., Xiao, Y., & Keywood, M., (2017). Shipborne  
 743 observations of the radiative effect of Southern Ocean clouds. *J. Geophys. Res. Atmos.*,  
 744 122, 318–328. doi.org/10.1002/2016JD026061.

749 Rauber, R. M., Ellis, S. M., Vivekanandan, J., Stith, J., Lee, W. C., McFarquhar, G. M., &  
 750 Janiszewski, A. (2017). Finescale structure of a snowstorm over the northeastern United  
 751 States: A first look at high-resolution HIAPER cloud radar observations. *Bull. Amer.*  
 752 *Meteor. Soc.*, 98(2), 253–269. doi.org/10.1175/BAMS-D-15-00180.1

753 Razenkov, I. A., E. W. Eloranta, J. P. Hedrick, R. E. Holz, R. E. Kuehn, and J. P. Garcia, 2002:  
 754 A high spectral resolution lidar designed for unattended operation in the Arctic. *Proc.*  
 755 *21st Int. Laser Radar Conf. (ILRC21)*, Quebec, QC, Canada, ICLAS, 57–64,  
 756 https://doi.org/10.1364/ORS.2001.OMC4

757 Schwartz, M. C., Ghate, V. P., Albrecht, B. A., Zuidema, P., Cadeddu, M. P., Vivekanandan, J.,  
 758 Ellis, S. M., Tsai, P., Eloranta, E. W., Mohrmann, J., Wood, R., & Bretherton, C. S.  
 759 (2019). Merged cloud and precipitation dataset from the HIAPER-GV for the Cloud  
 760 System Evolution in the Trades (CSET) Campaign. *J. Atmos. Oceanic Technol.*, 36, 921-  
 761 940. doi.org/10.1175/JTECH-D-18-0111.1

762 Shupe, M. D. (2007). A ground based multisensory cloud phase classifier. *J. Geophys. Res.*  
 763 *Atmos.* 34, L22809. doi.org/10.1029/2007GL031008

764 Shupe, M. D., Comstock, J. M., Turner, D. D., & Mace, G. G. (2016). Cloud property retrievals  
 765 in the ARM Program, in The Atmospheric Radiation Measurement Program: The First 20  
 766 Years. *Meteor. Monogr.*, 19.1–19.20. doi.org/10.1175/AMSMONOGRAPHS-D-15-  
 767 0030.1

768 Silber, I., Verlinde, J., Eloranta, E. W., & Cadeddu, M. (2018). Antarctic cloud macrophysical,  
 769 thermodynamic phase, and atmospheric inversion coupling properties at McMurdo  
 770 Station. Part I: Principal data processing and climatology. *J. Geophys. Res. Atmos.*, 123,  
 771 6099–6121. doi.org/10.1029/2018/JD028279

772 Simmonds, I., & Keay, K. (2000). Mean southern hemisphere extratropical cyclone behavior in  
 773 the 40-year NCEP–NCAR reanalysis. *J. Clim.*, 13(5), 873–885.  
 774 doi.org/10.1175/1520/0442(2000)013<0873:MSHECB>2.0.CO;2

775 Spinhirne J. D., Hansen, M. Z., Caudill, L. O. (1982). Cloud Top Remote Sensing by Airborne  
 776 Lidar. *Applied Optics*, 21(9) 1564-1571. doi.org/10.1364/AO.21.001564

777 Tan, I., Storelvmo, T., & Zelinka, M. D. (2016). Observational constraints on mixed-phase  
 778 clouds imply higher climate sensitivity. *Science*, 352(6282), 224-  
 779 227. <https://doi.org/10.1126/science.aad5300>

780 Thorsen, T. J., Fu, Q., Newsom, R. K., Turner, D. D., & Comstock, J. M. (2015). Automated  
 781 retrieval of cloud and aerosol properties from the ARM Raman Lidar. Part I: Feature  
 782 detection. *J. Atmos. Oceanic Technol.*, 32(11), 1977–1998. doi.org/10.1175/JTECH-D-  
 783 14-00150.1

784 UCAR 2020: AVAPS Dropsondes <https://www.eol.ucar.edu/content/avaps-dropsondes>, Accessed  
 785 30 July 2020.

786 Um, J., McFarquhar, G. M., Stith, J. L., Jung, C. H., Lee, S. S., Lee, J. Y., Shin, Y., Lee, Y. G.,  
 787 Yang, Y. I., Yum, S. S., Kim, B-G., Cha, J. W., & Ko, A-R. (2018). Microphysical  
 788 characteristics of frozen droplet aggregates from deep convective clouds. *Atmos. Chem.*  
 789 *Phys.*, 18, 16915-16930. <https://doi.org/10.5194/acp-18-16915-2018>  
 790 Wang, Y., McFarquhar, G. M., Rauber, R. M., Zhao, C., Wu, W., Finlon, J. A., Stechman, D. M.,  
 791 Stith, J., Jensen, J. B., Schnaiter, M., Järvinen, E., Waitz, F., Vivekanandan, J., Dixon,  
 792 M., Rainwater, B., & Toohey, T. (2020). Microphysical properties of generating cells  
 793 over the Southern Ocean: Results from SOCRATES. *J. Geophys. Res. Atmos.*, 125,  
 794 e2019JD032237. <https://doi.org/10.1029/2019JD032237>  
 795 Wang, Z., French, J., Vali, G., Wechsler, P., Haimov, S., Rodi, A., Deng, M., Leon, D., Snider,  
 796 J., & Peng, L. (2012). Single aircraft integration of remote sensing and in situ sampling  
 797 for the study of cloud microphysics and dynamics. *Bull. Amer. Meteor. Soc.*, 93, 653–  
 798 668. [doi.org/10.1175/BAMS-D-11-00044.1](https://doi.org/10.1175/BAMS-D-11-00044.1).  
 799 Winker, D. M., Vaughan, M. A., Omar, A., Hu, Y., & Powell, K. A. (2009). Overview of the  
 800 CALIPSO Mission and CALIOP data processing algorithms. *J. Atmos. Oceanic Technol.*,  
 801 26(11), 2310-2323. <https://doi.org/10.1175/2009JTechA1281.1>  
 802

## **Acknowledgments:**

This work was supported by the National Science Foundation (Grant AGS 1628674 and AGS 1762096). We appreciate the efforts of the entire SOCRATES team in collecting a high-quality dataset. We especially appreciate the efforts of Dr. Michael Dixon and Dr. Ulrike Romatschke in quality controlling the HCR dataset and building the merged 2 Hz HCR/HSRL dataset. We also would like to thank Dr. Scott Ellis and Dr. Jothiram Vivekanandan for answering our questions regarding the HCR. We also thank Dr. Alain Protat and an anonymous reviewer for comments which helped substantially improve the quality of the paper.

## **Data Availability**

The data that support the findings of this study can be obtained at the following addresses:

2DS data: <https://doi.org/10.26023/8HMG-WQP3-XA0X>

Flight-level data (e.g., RICE, CDP, navigation data): <https://doi.org/10.5065/D6M32TM9>

HCR radar time series data: <https://doi.org/10.5065/D6D7998S>

Dropsonde data: <https://doi.org/10.5065/D6QZ28SG>

HSRL data: <https://doi.org/10.5065/D64J0CZS>

820 Table 1: High-Altitude Flight Leg Start/End Times and Number of Dropsondes Deployed

<i>Research Flight</i>	Start Time	End Time	Dropsondes Deployed	Dropsonde Maximum Horiz. Displacement	Avg. Dist. Between Dropsondes Deployed	GV Track Length
RF02	2018-01-19 01:33:00 UTC	2018-01-19 03:24:00 UTC	7	5.5 – 11 km	221.6 km	1313 km
RF03	2018-01-22 21:39:00 UTC	2018-01-22 23:44:00 UTC	6	4.3 – 13 km	284.7 km	1401 km
RF04	2018-01-24 00:06:00 UTC	2018-01-24 01:58:00 UTC	7	1.4 – 15.9 km	232.6 km	1347 km
RF05	2018-01-25 23:07:00 UTC	2018-01-26 00:46:00 UTC	5	7.3 – 11 km	307.8 km	1199 km
RF06	2018-01-28 23:40:00 UTC	2018-01-29 01:19:00 UTC	7	5.4 – 10.5 km	223.1 km	1297 km
RF07	2018-01-31 01:37:00 UTC	2018-01-31 03:15:00 UTC	6	4.3 – 7.4 km	228.1 km	1112 km
RF10	2018-02-07 21:30:00 UTC	2018-02-07 23:55:00 UTC	7	5.6 – 9.5 km	175.5 km	1543 km
RF11	2018-02-17 02:15:00 UTC	2018-02-17 03:02:00 UTC	7	7.3 – 13 km	96.5 km	536 km
RF12	2018-02-18 00:30:00 UTC	2018-02-18 02:38:00 UTC	7	7.2 – 9.5 km	157 km	1233 km
RF13	2018-02-19 23:40:00 UTC	2018-02-20 01:30:00 UTC	10	3.87 – 5.7 km	138.6 km	1106 km
RF14	2018-02-21 23:18:00 UTC	2018-02-22 01:45:00 UTC	14	3 – 13.1 km	117 km	1497 km
RF15	2018-02-24 02:26:00 UTC	2018-02-24 03:52:00 UTC	11	9.7 – 13.3 km	89.5 km	787.5 km

823  
824

**Table 2: Time Periods Used to Build Aerosol Training Dataset**

<i>Research Flight</i>	<b>Start Time</b>	<b>End Time</b>
<i>RF02</i>	2018-01-19 01:52:15 UTC	2018-01-19 01:56:00 UTC
<i>RF02</i>	2018-01-19 02:08:00 UTC	2018-01-19 02:14:55 UTC
<i>RF02</i>	2018-01-19 02:43:00 UTC	2018-01-19 02:50:55 UTC
<i>RF03</i>	2018-01-22 22:06:15 UTC	2018-01-22 22:08:15 UTC
<i>RF05</i>	2018-01-25 23:50:15 UTC	2018-01-25 23:52:45 UTC
<i>RF05</i>	2018-01-25 23:54:45 UTC	2018-01-25 23:58:45 UTC
<i>RF05</i>	2018-01-26 00:00:45 UTC	2018-01-26 00:03:00 UTC
<i>RF05</i>	2018-01-26 00:08:15 UTC	2018-01-26 00:23:30 UTC
<i>RF05</i>	2018-01-26 00:24:00 UTC	2018-01-26 00:32:30 UTC
<i>RF05</i>	2018-01-26 00:37:45 UTC	2018-01-26 00:43:30 UTC
<i>RF05</i>	2018-01-26 00:48:30 UTC	2018-01-26 00:54:00 UTC
<i>RF06</i>	2018-01-28 23:40:00 UTC	2018-01-28 23:44:00 UTC
<i>RF06</i>	2018-01-28 23:58:11 UTC	2018-01-29 00:18:26 UTC
<i>RF06</i>	2018-01-29 00:22:30 UTC	2018-01-29 00:27:30 UTC
<i>RF06</i>	2018-01-29 00:33:45 UTC	2018-01-29 00:44:00 UTC
<i>RF06</i>	2018-01-29 00:49:30 UTC	2018-01-29 00:55:30 UTC
<i>RF12</i>	2018-02-17 02:42:15 UTC	2018-02-17 02:44:00 UTC
<i>RF14</i>	2018-02-21 23:17:00 UTC	2018-02-21 23:22:00 UTC
<i>RF14</i>	2018-02-22 00:43:00 UTC	2018-02-22 00:45:30 UTC

825  
826

827

Table 3: Cloud top phase by Research Flight

<b>Research Flight</b>	<b>Liquid</b>	<b>Ice</b>	<b>Uncertain</b>	<b>Number of Cloud Containing Columns</b>	<b>Number of Cloud Top Elements</b>
<i>RF02</i>	95.5%	0.3%	4.2%	9,046	40,029
<i>RF03</i>	59.0%	2.1%	38.8%	8,065	35,913
<i>RF04</i>	80.2%	1.3%	18.4%	7,924	36,558
<i>RF05</i>	97.7%	0.1%	2.2%	3,127	13,159
<i>RF06</i>	93.1%	1.6%	5.3%	3,362	12,448
<i>RF07</i>	85.4%	2.8%	11.9%	5,957	23,781
<i>RF10</i>	90.3 %	1.5%	8.2%	12,097	53,371
<i>RF11</i>	79.6%	0.7%	19.8%	3,825	16,810
<i>RF12</i>	92.8%	1.1%	6.1%	13,374	59,266
<i>RF13</i>	96.0%	2.7%	1.2%	13,197	42,996
<i>RF14</i>	91.6%	0.5%	7.9%	15,735	68,830
<i>RF15</i>	82.2%	1.7%	16.1%	7,993	33,731
<i>All RF</i>	87.5%	1.4%	11.2%	103,702	436,892

828

829

830

Table 4: Phase of Elements Beneath Cloud Top

<i>Phase Detection</i>	<b>1</b> <b>(0 – 19.2 m)</b>	<b>2</b> <b>(19.2 - 38.4 m)</b>	<b>3</b> <b>(38.4 – 57.6</b> <b>m)</b>	<b>4</b> <b>(57.6 – 76.8</b> <b>m)</b>	<b>5</b> <b>(76.8 - 96 m)</b>	<b>All Cloud Top</b> <b>Elements</b>
<i>Liquid</i>	85.6%	90.5%	90.6%	87.0%	82.3%	87.5%
<i>Ice</i>	2.1%	0.4%	0.5%	1.7%	2.3%	1.4%
<i>Uncertain</i>	12.3%	9.1%	8.9%	11.4%	15.4%	11.2%

831

832



833

Table 5: Cloud Top Phase by Cloud Top Temperature

<i>Cloud Top Temperatures</i>	Liquid	Ice	Uncertain	Percentage of Cloud Top Elements	Number of Cloud Top Columns	Percentage of Cloud Top Columns
-30 to -25°C	52.8%	1.9%	45.2%	3.2%	3,062	3%
-25 to -20°C	48.3%	4.1%	47.7%	2.8%	2,713	2.6%
-20 to -15°C	72.3%	1.3%	26.4%	3.6%	3,311	3.2%
-15 to -10°C	78.2%	0.7%	21.1%	7.6%	7,033	6.8%
-10 to -5°C	93.2%	1%	5.8%	14.6%	14,014	13.5%
-5 to 0°C	90.6%	1.9%	7.6%	39.1%	39,691	38.3%
0 to 5°C	94.8%	0%	5.2%	21.6%	25,034	24.1%
5 to 10°C	88.1%	0%	11.9%	7.1%	8,431	8.1%
10 to 15°C	91%	0%	9%	0.3%	413	0.4%

834

835

## Figures

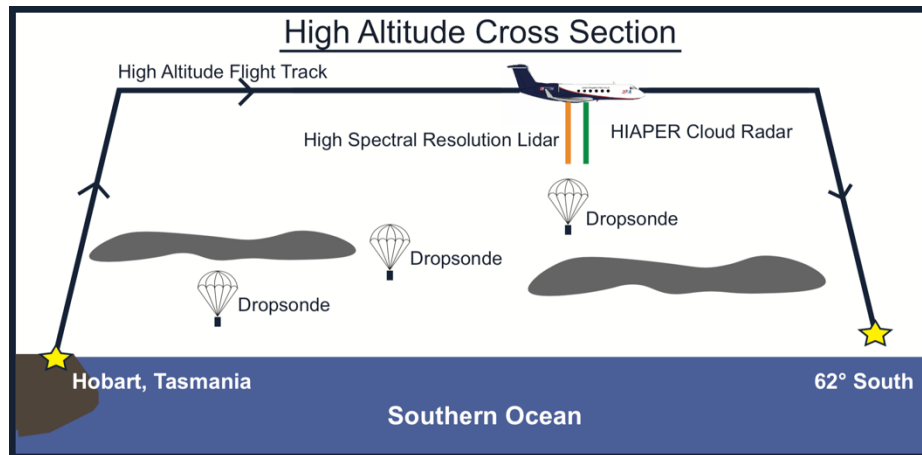


Fig. 1: Vertical cross section showing a typical high-altitude cross section from Hobart, Tasmania to approximately 62°S during SOCRATES.

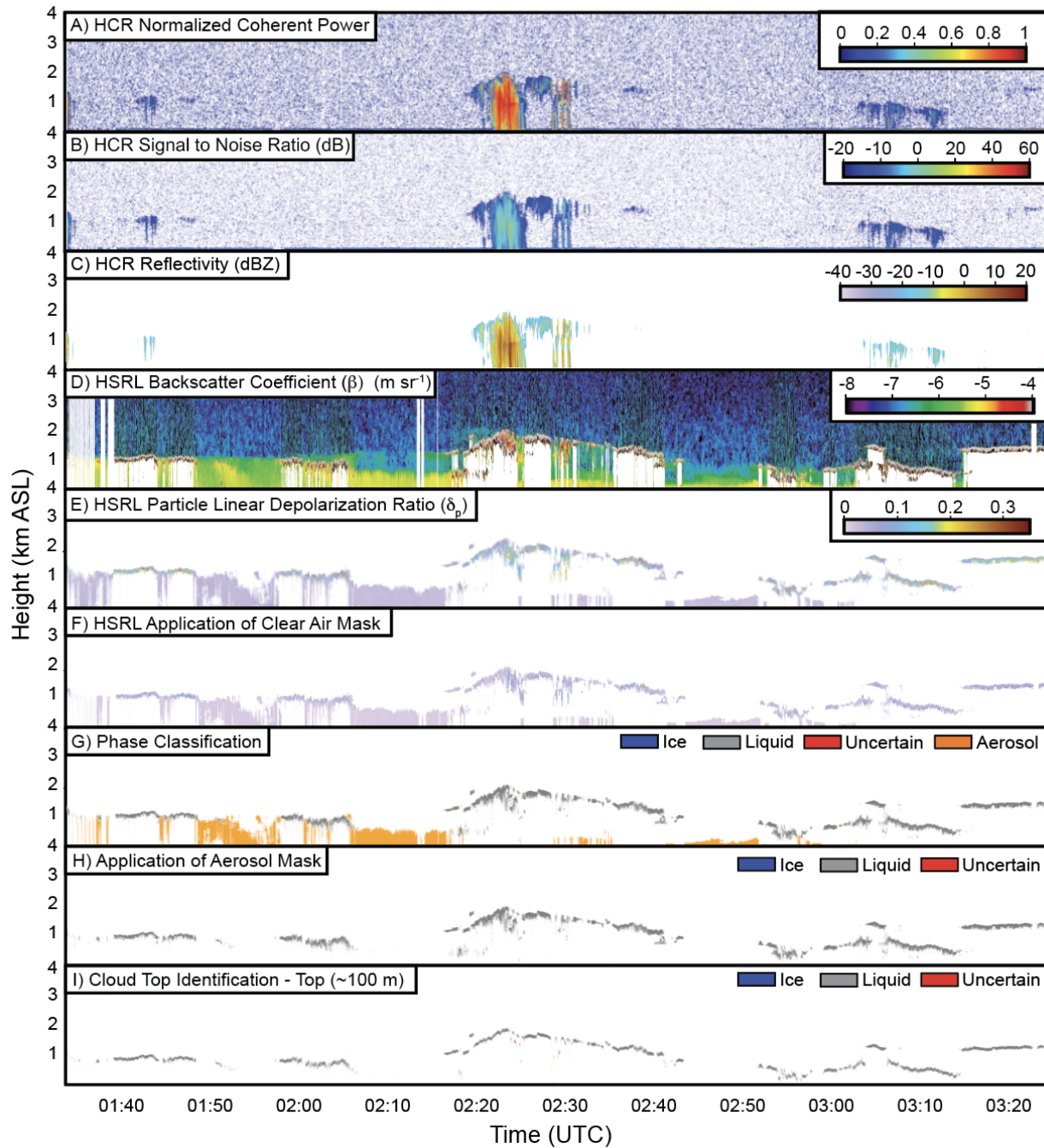


Fig. 2: An example from the RF02 high altitude flight leg showing the processing of the merged HCR/HSRL data. Time is in UTC and height is in km above sea level (ASL). A) NCP, B) SNR, C)  $Z_e$ , D)  $\beta$  from the HCR and HSRL merged dataset, respectively, before processing, E)  $\delta_p$ , F) HSRL data following application of the clear air mask, G) results of the phase classification, H) application of the aerosol mask, and I) final cloud top phase classification.

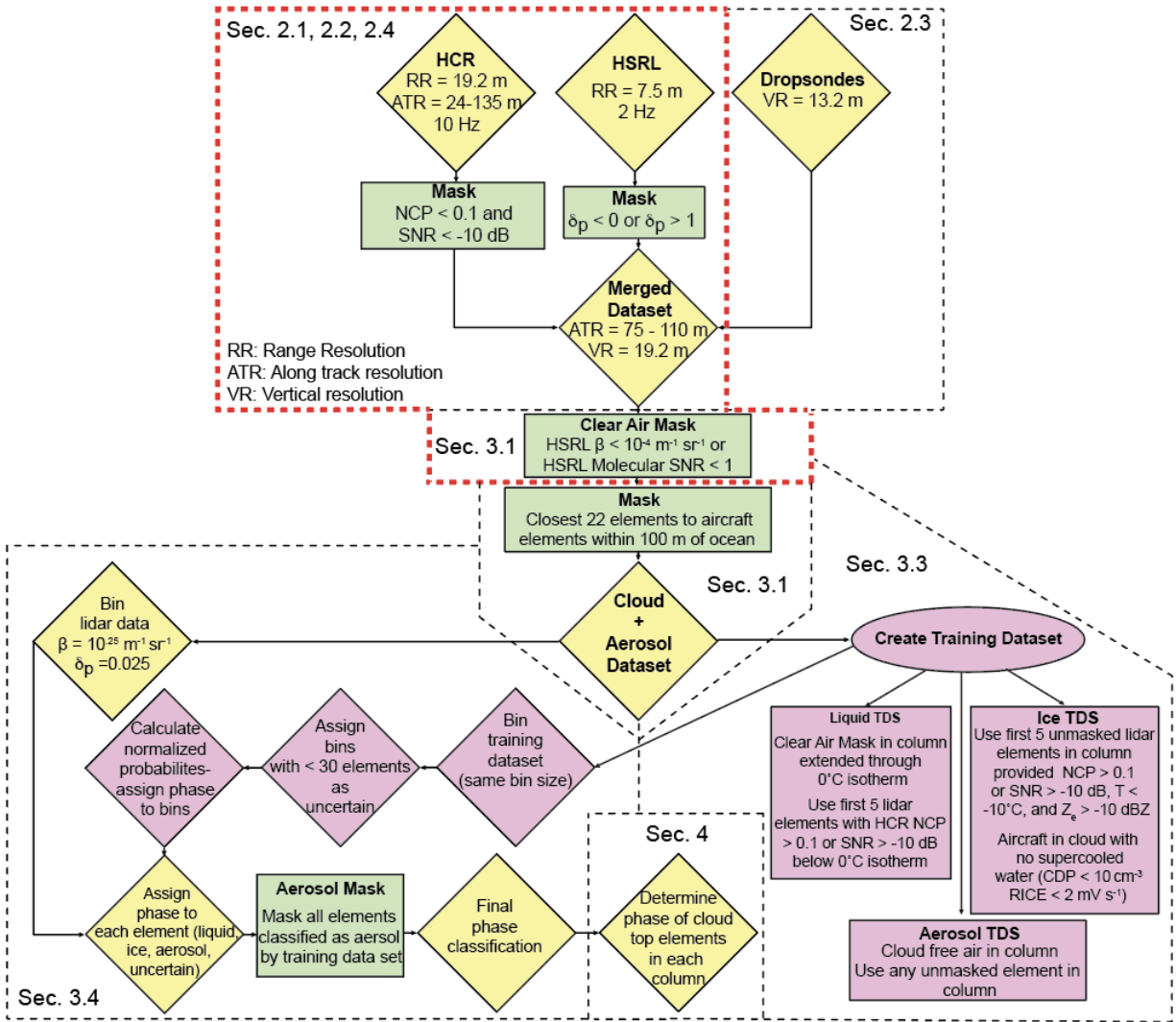
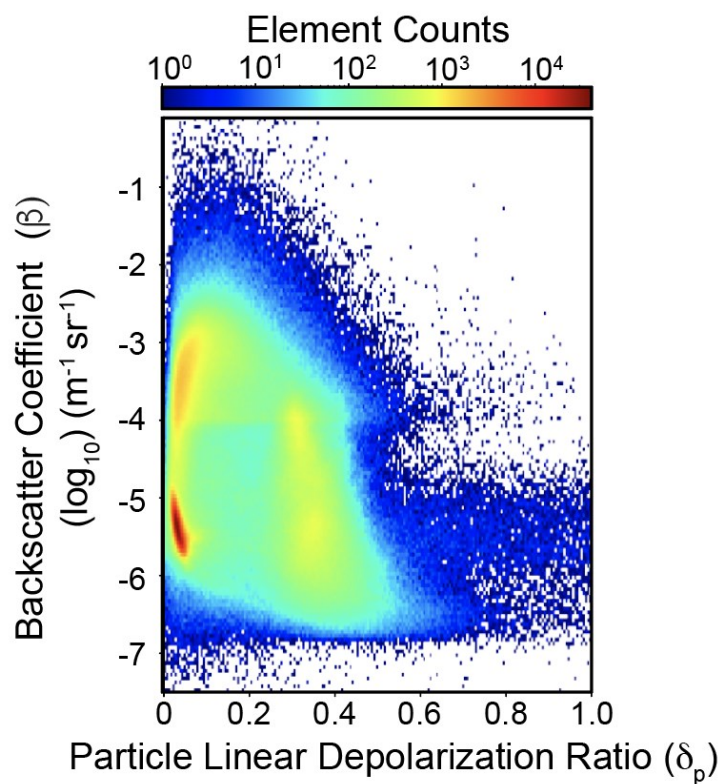


Fig. 3. Flow chart summarizing phase identification algorithm. Processing steps taken by NCAR are denoted by the red dashed box.

853



854

855 Fig. 4: Two-dimensional histogram showing particle linear depolarization ratio ( $\delta_p$ ) and aerosol  
 856 backscatter coefficient ( $\beta$ ) of all elements from the twelve high-altitude flight legs. The bin width  
 857 was 0.01  $\delta_p$  and  $\beta$  of  $0.1 \text{ m}^{-1} \text{sr}^{-1}$   
 858

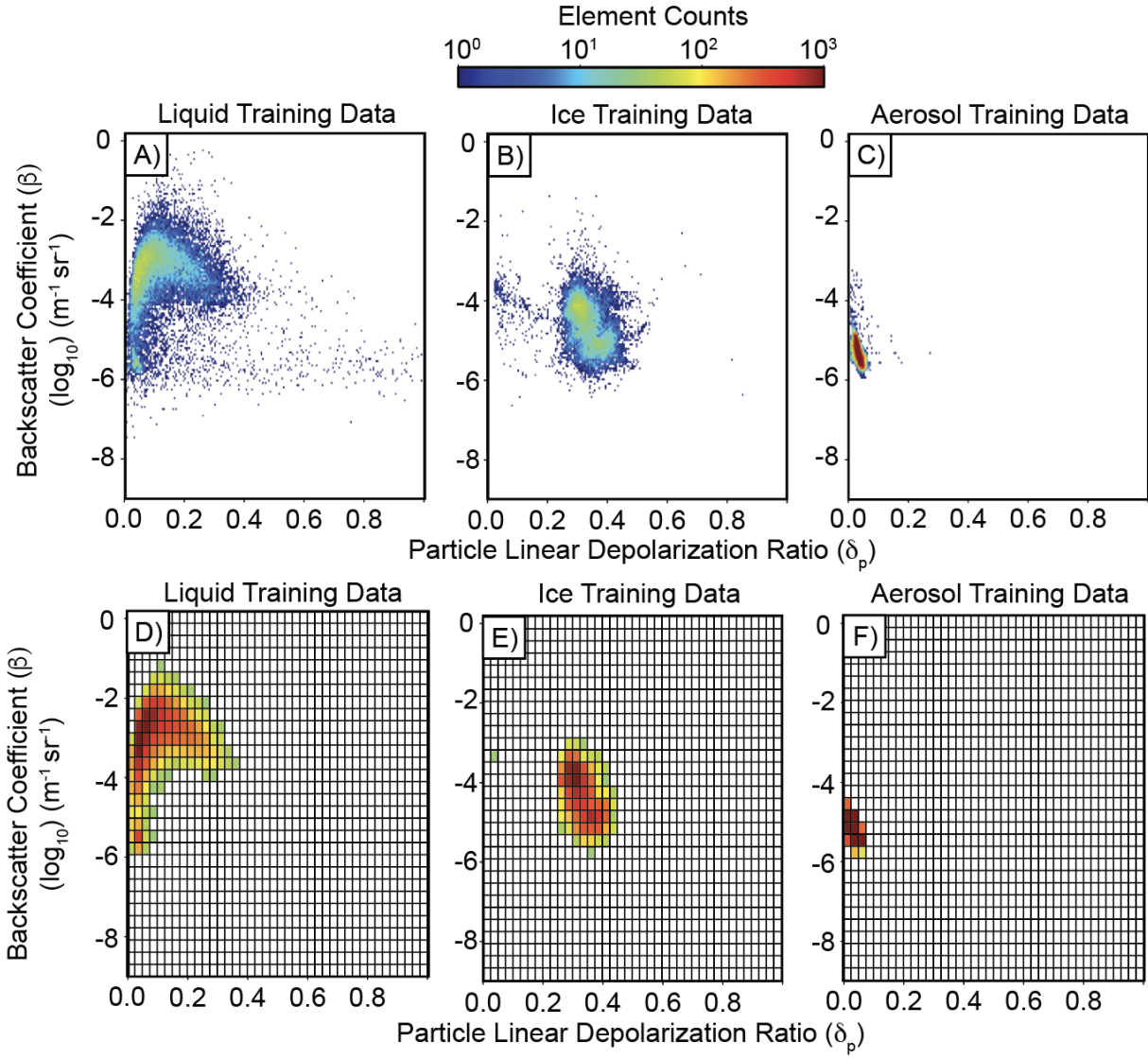


Fig. 5: Two-dimensional histograms of the training dataset: (A) cloud liquid, (B) cloud ice, and (C) aerosol. The bin width for A-C was  $0.01 \delta_p$  and  $\beta$  of  $0.1 \text{ m}^{-1} \text{ sr}^{-1}$ . The training dataset was gridded into bins (D-F) such that each bin has a  $\delta_p$  of  $0.025$  and  $\beta$  of  $0.25 \text{ m}^{-1} \text{ sr}^{-1}$ . Bins containing less than 30 elements were not used in the training dataset.

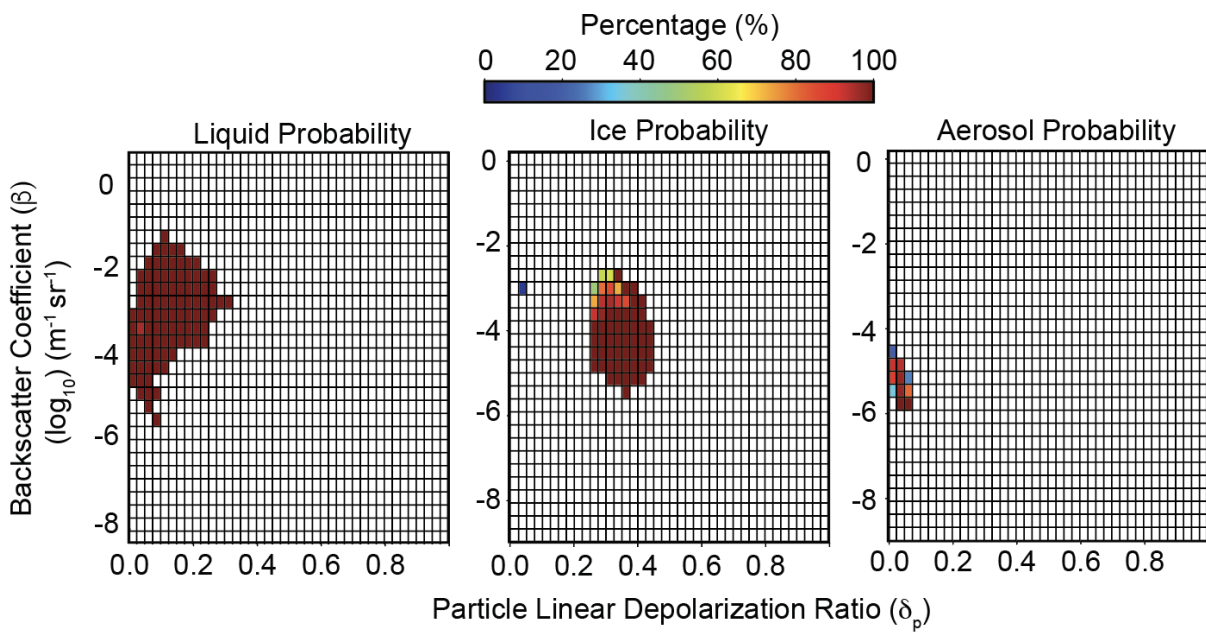


Fig. 6: Probability calculated using methodology discussed in Sec. 3.4

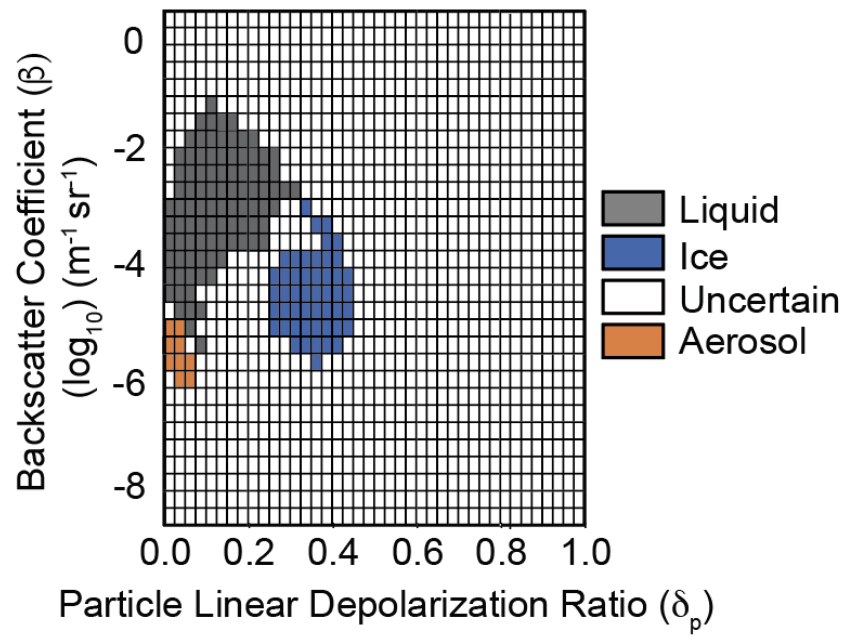
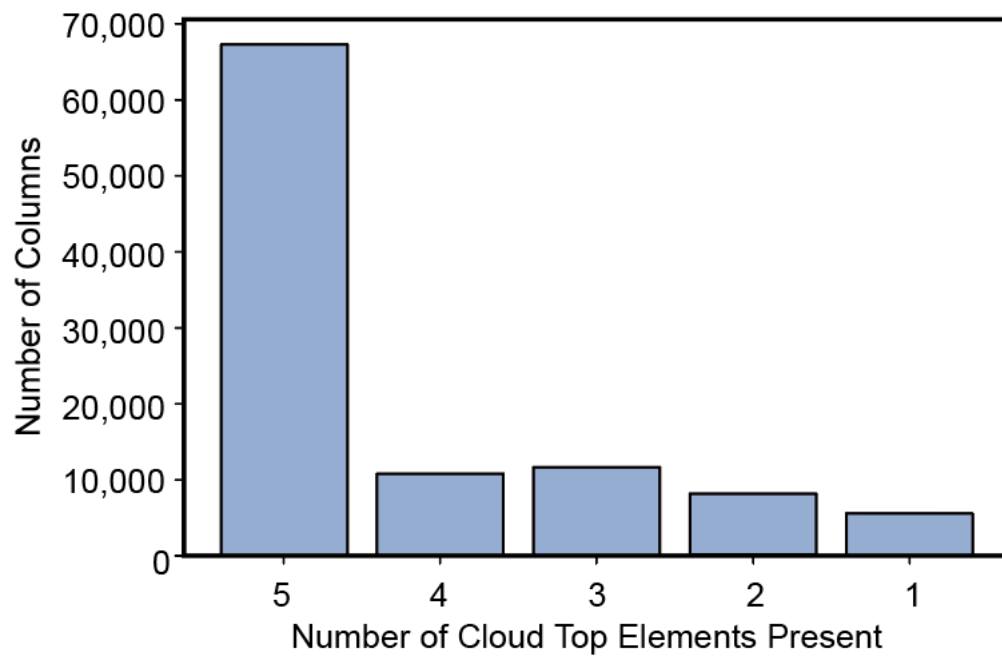


Fig. 7: Final phase classification based on a probability threshold  $> 0.95$  for cloud liquid, cloud ice, and deliquesced aerosol.





872

873 Fig. 8: Number of elements present in the cloud top layer. Five elements present would indicate  
874 cloud depth  $\geq 96$  m. Clouds with less than five elements represent thin clouds with depths less  
875 than 96 m.

876

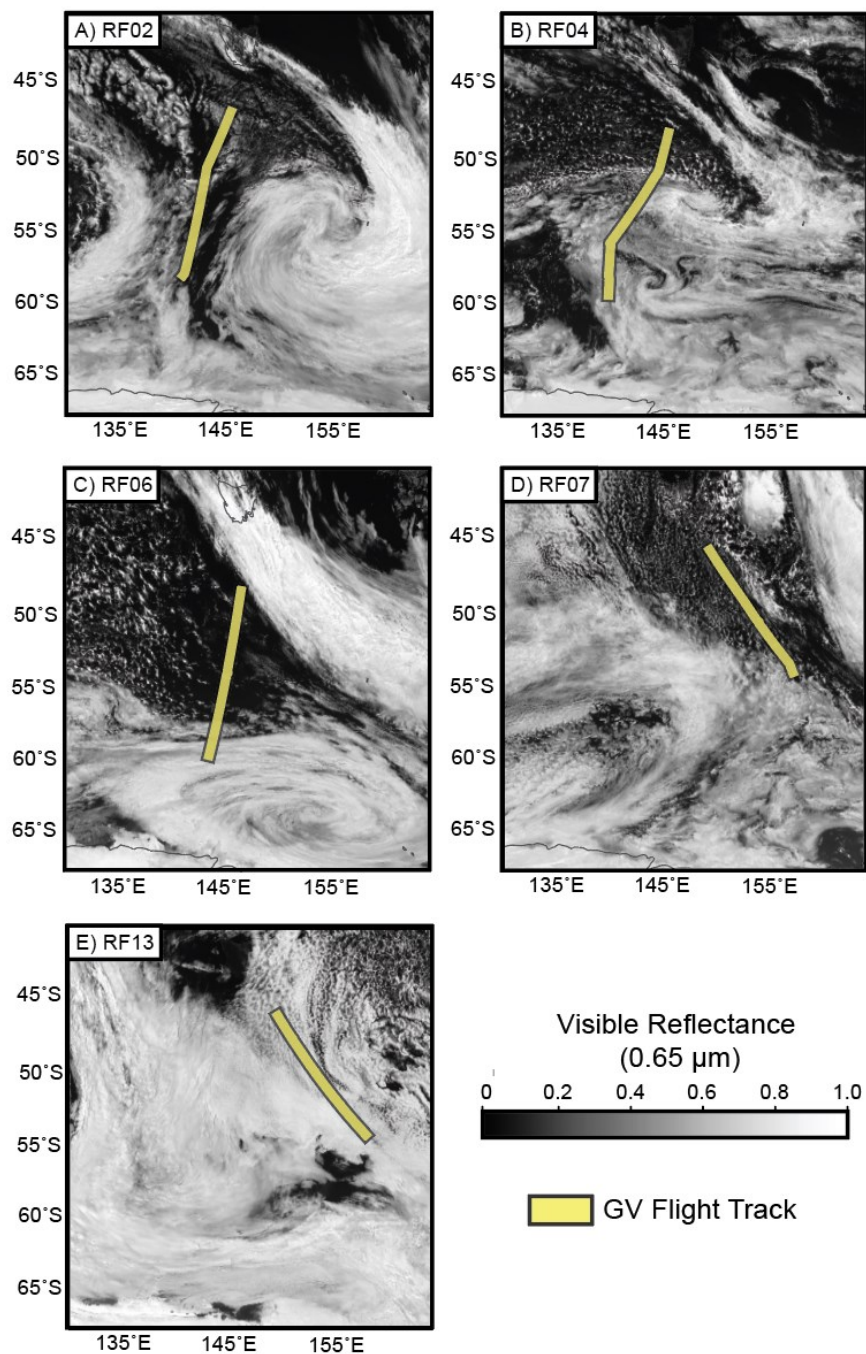


Fig. 9: Visible reflectance from the Himawari-8 satellite from A) RF02 valid at 19 January 2018 02:30 UTC, B) RF04 valid at 24 January 2018 02:00 UTC, C) RF06 valid at 29 January 2018 01:00 UTC, D) RF07 valid at 31 January 2018 02:20 UTC, E) RF13 valid at February 2018 00:40 UTC. High-altitude flight track is in yellow.

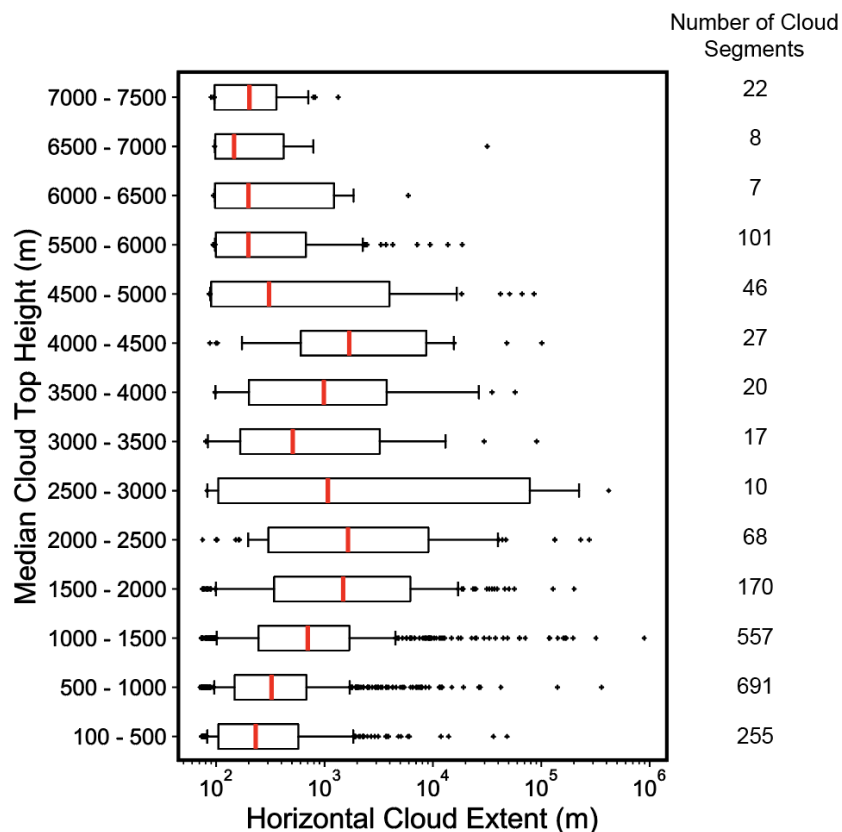


Fig. 10: Box and whisker plot of horizontal cloud extent during high-altitude flight legs broken down by median cloud top height (500 m intervals). At each 500 m interval, the box represents the 25<sup>th</sup> and 75<sup>th</sup> quantiles of the horizontal cloud extent and the median value is denoted by a red line within the box. Whiskers extend to a the 10<sup>th</sup> and 90<sup>th</sup> quantiles. Outliers/extreme values are denoted by a +. The number of sampled cloud segments in each 500 m altitude range is located to the right of the figure. Horizontal cloud extent is on a logarithmic scale.

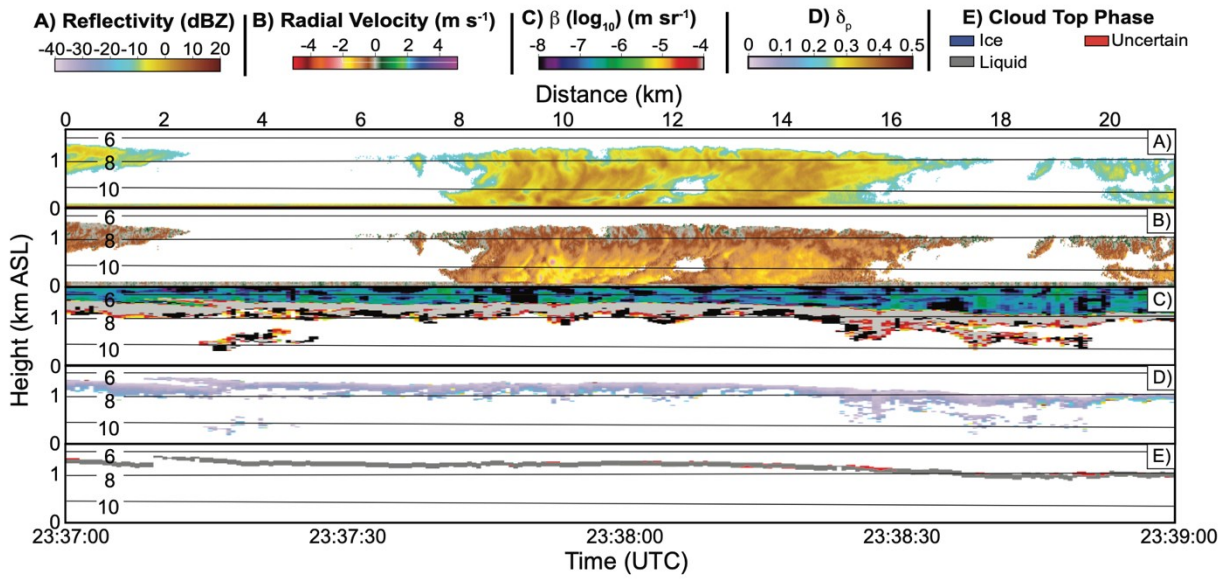


Fig. 11: RF14 10 Hz HCR (A)  $Z_e$ , (B)  $V_r$ , (C) 2 Hz  $\beta$ , and (D) 2 Hz  $\delta_p$  data from 23:37:00 to 23:39:00. The fifth time series (E) shows 2 Hz cloud top phase. Temperature (°C) is overlaid.

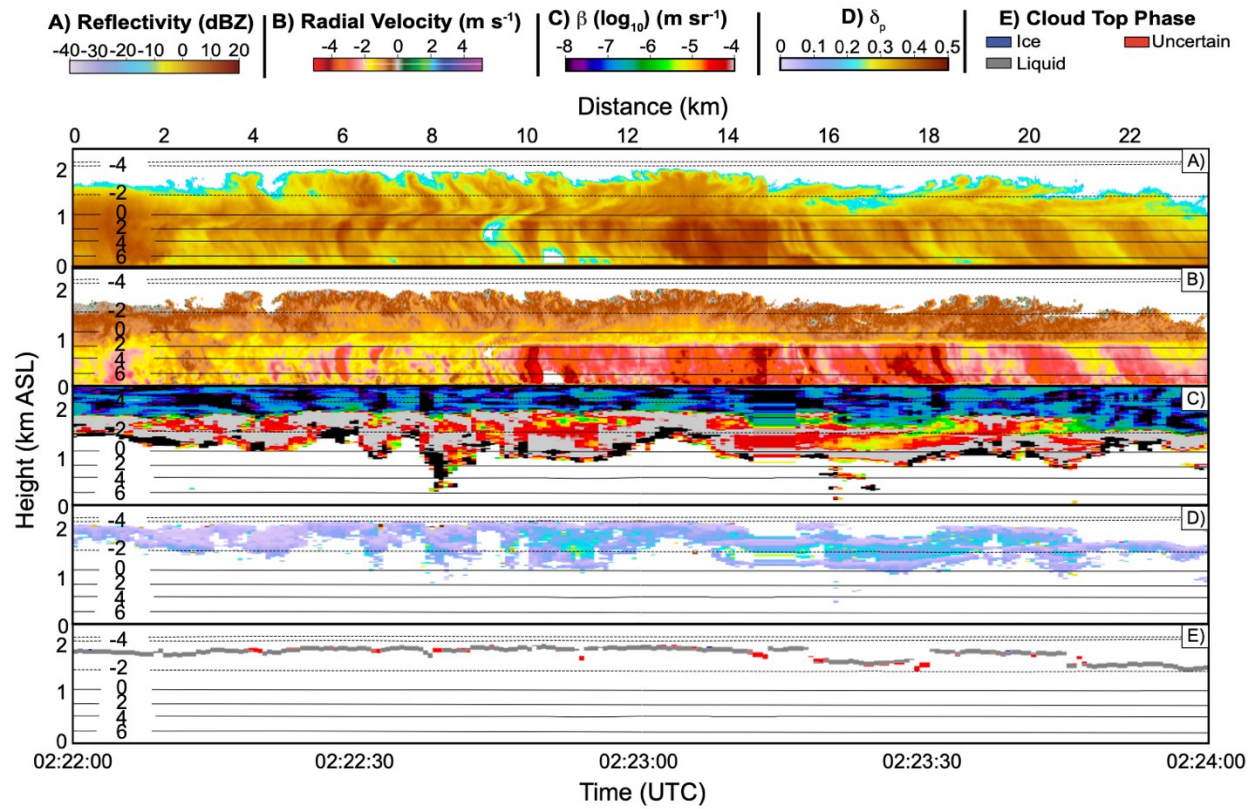


Fig. 12: Same as Fig. 11, but for RF02 from 02:22:00 to 02:24:00. A temperature inversion is present at -4°C.

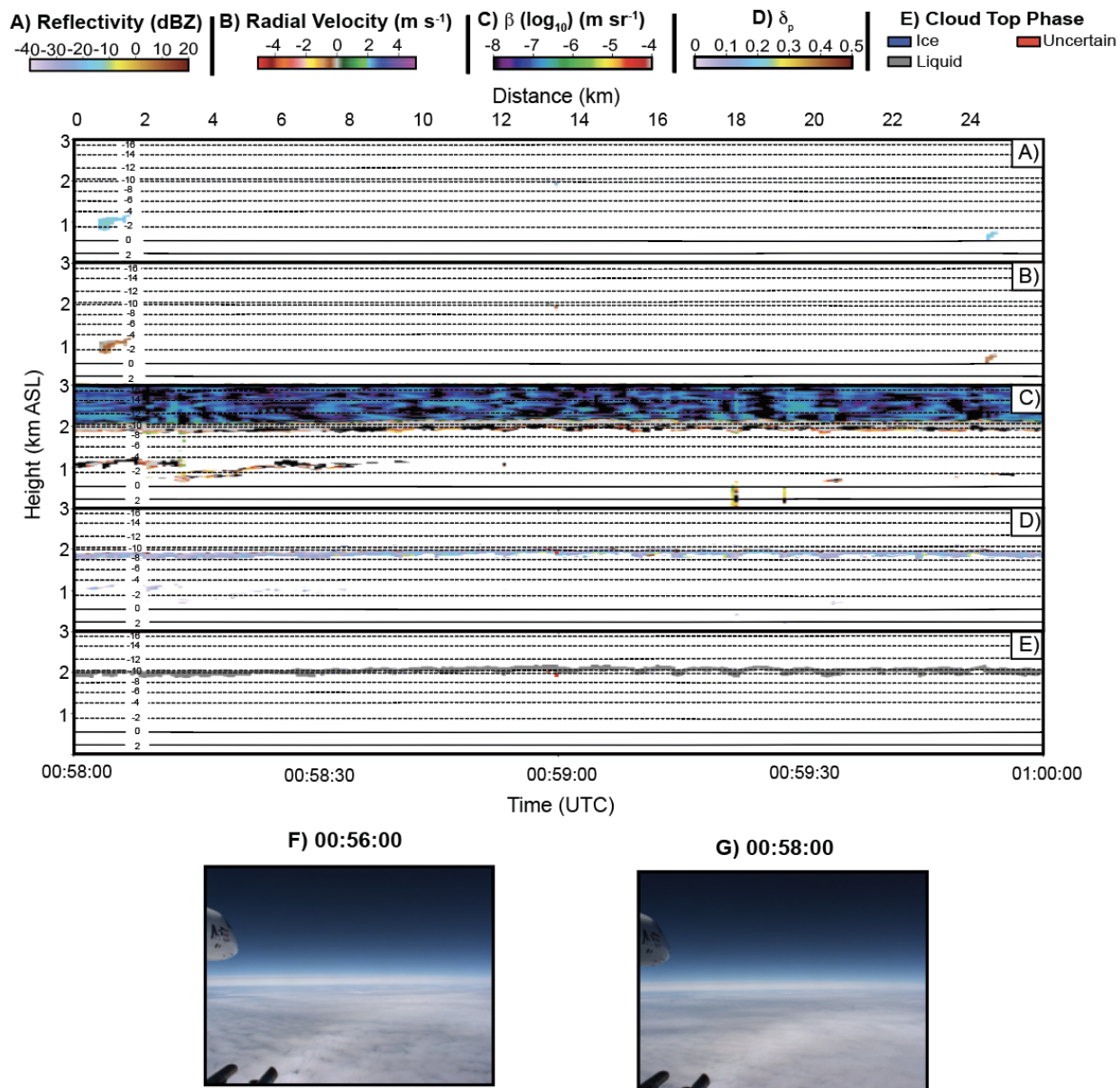


Fig. 13: Same as Fig 11, but for RF06 from 00:58:00 to 01:00:00. Forward facing flight level imagery shown at 00:56:00 (F) and 00:58:00 (G). A temperature inversion is present at -10°C.



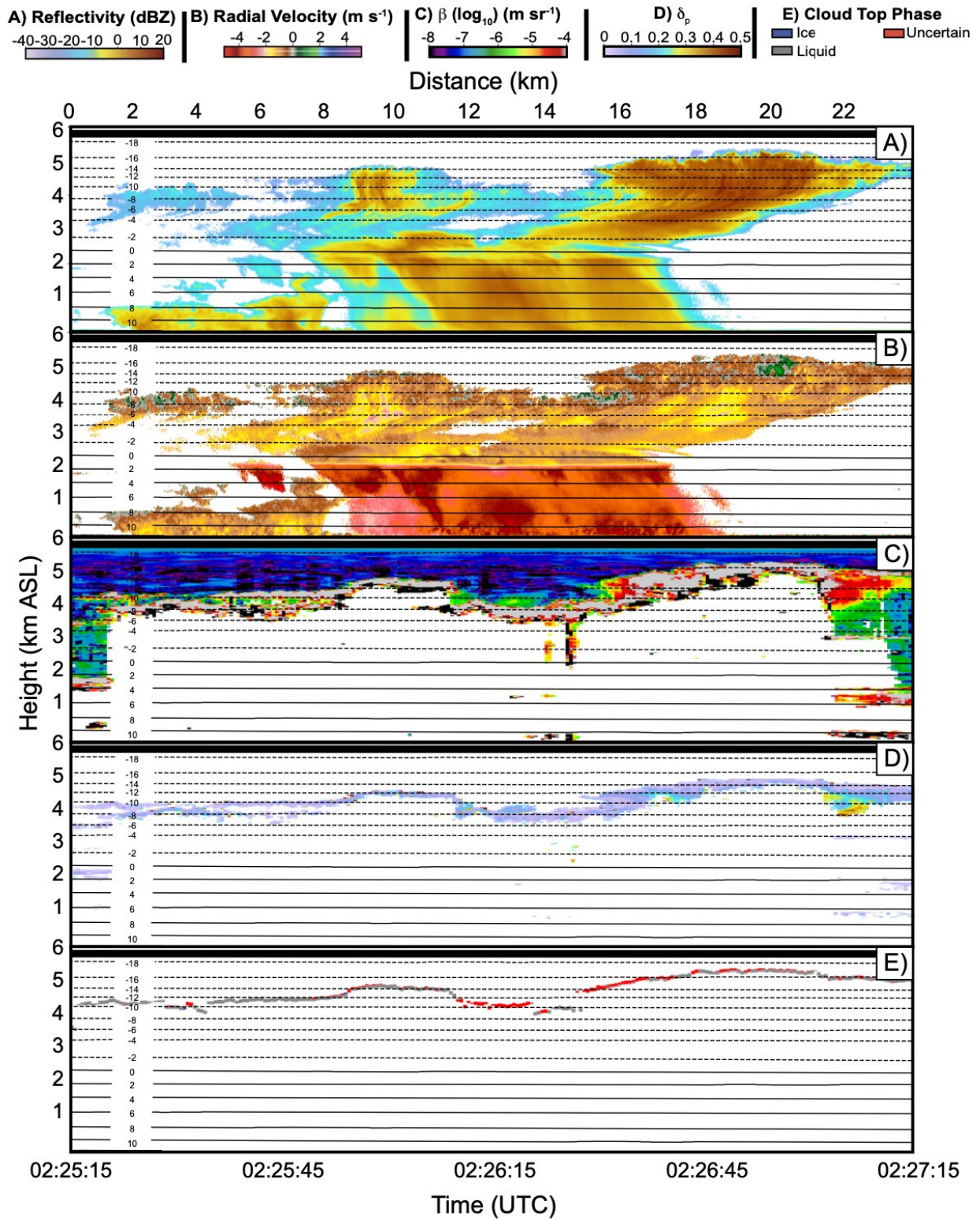


Fig. 14: Same as Fig. 11, but for RF11 from 02:25:15 to 02:27:15.

907

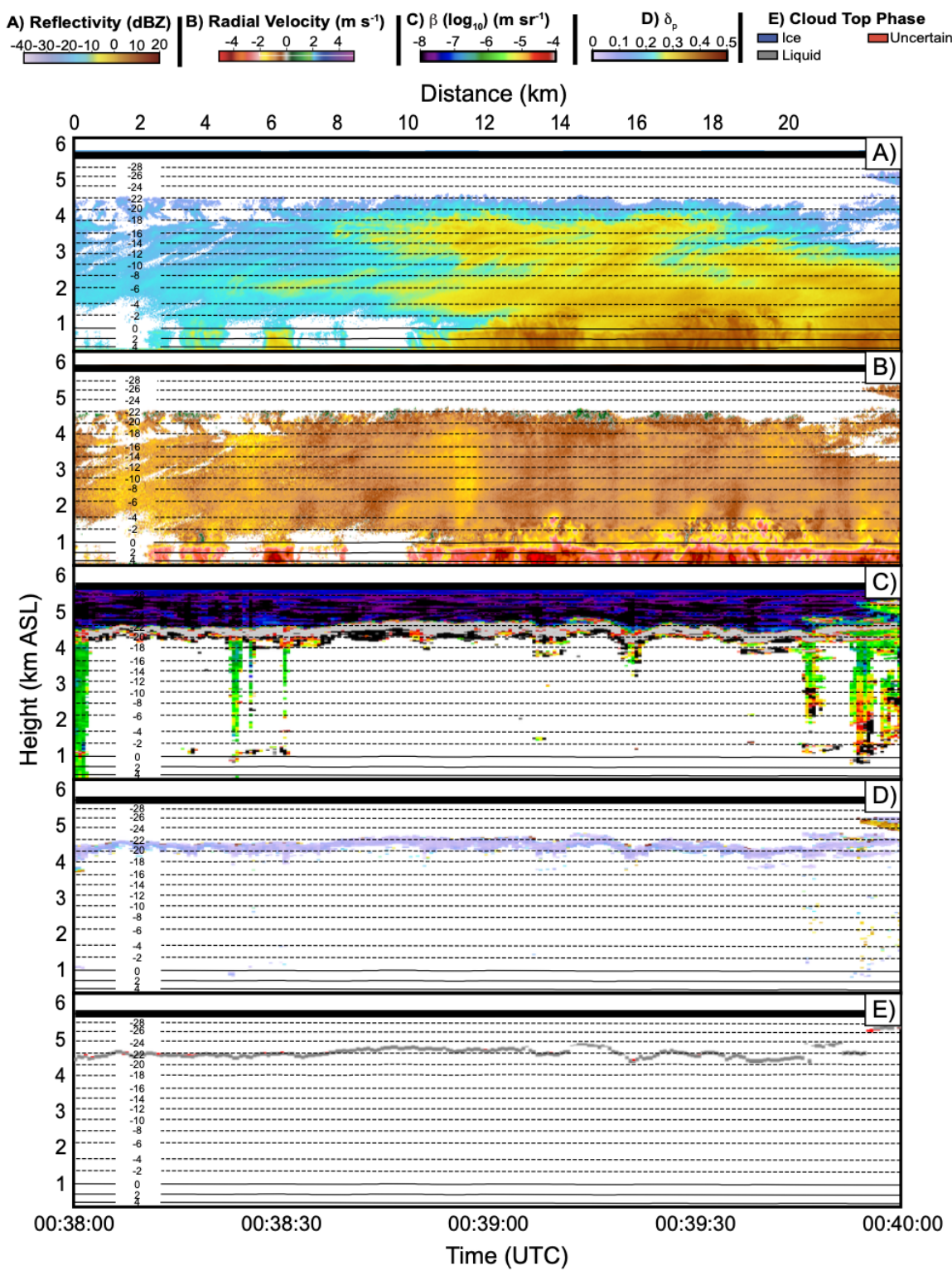


Fig. 15: Same as Fig. 11, but for RF04 from 00:38:00 UTC to 00:40:00 UTC.



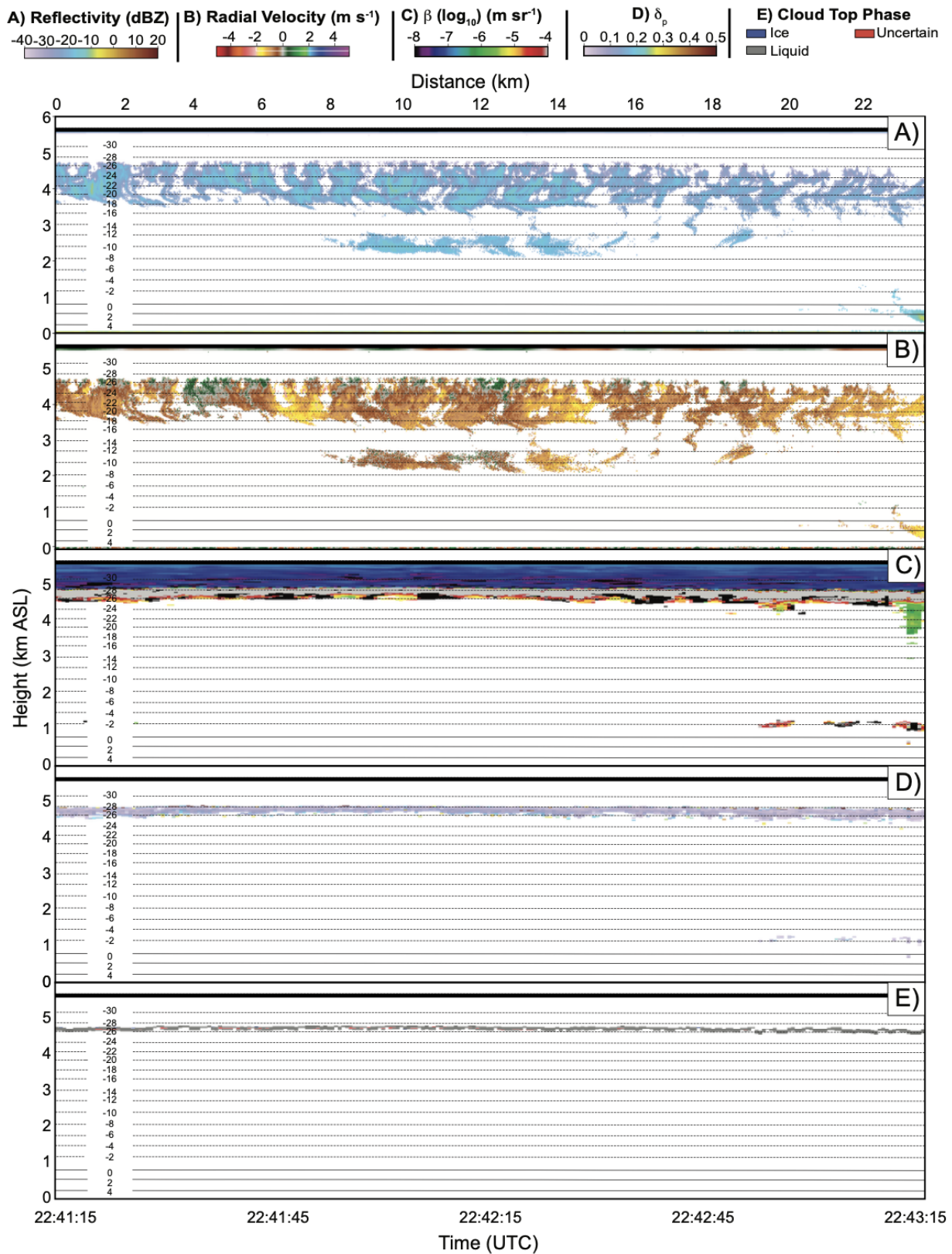


Fig. 16: Same as Fig. 11, except for RF03 from 22:41:15 UTC to 22:43:15 UTC.

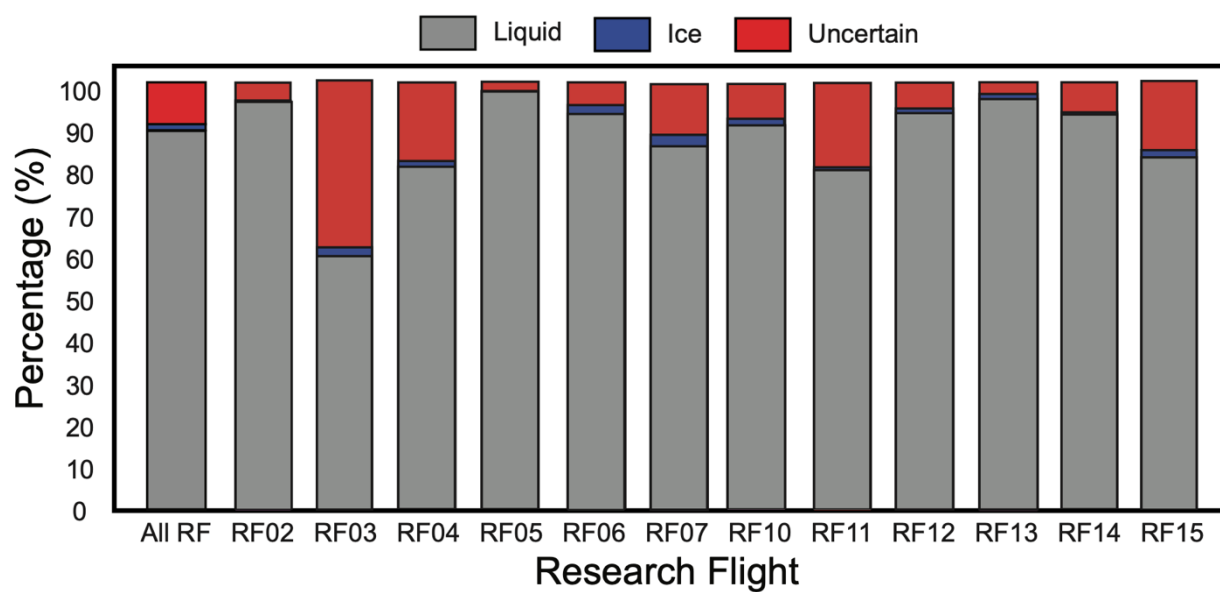


Fig. 17: Cloud top phase classification for individual flights and entire dataset (see also Table 3).

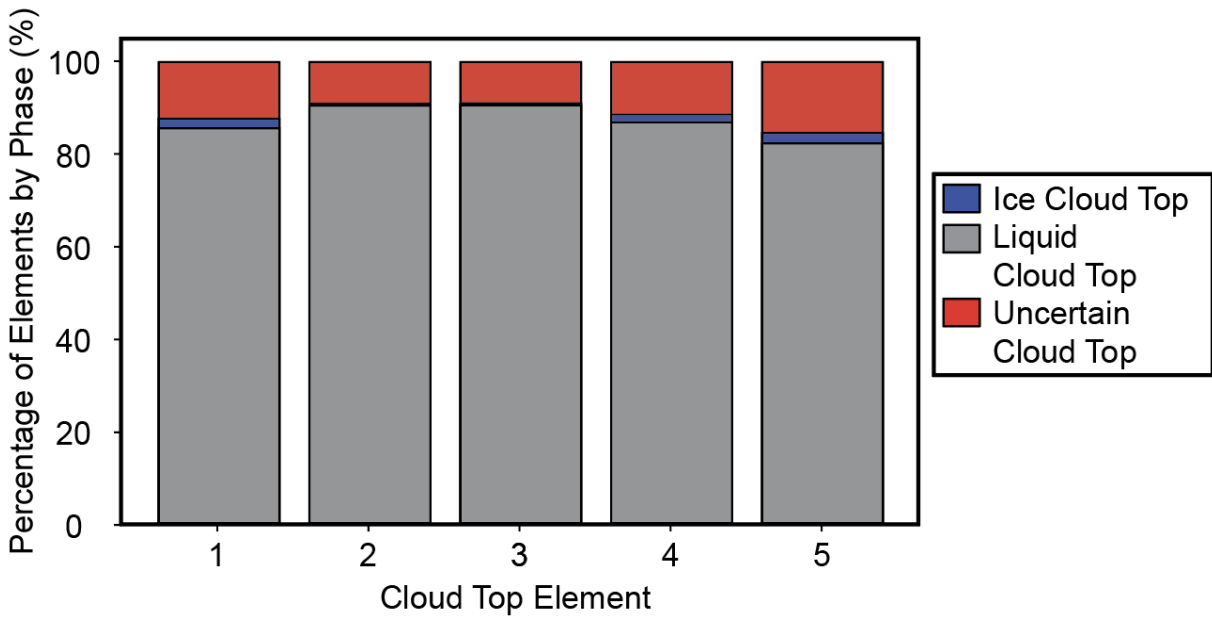
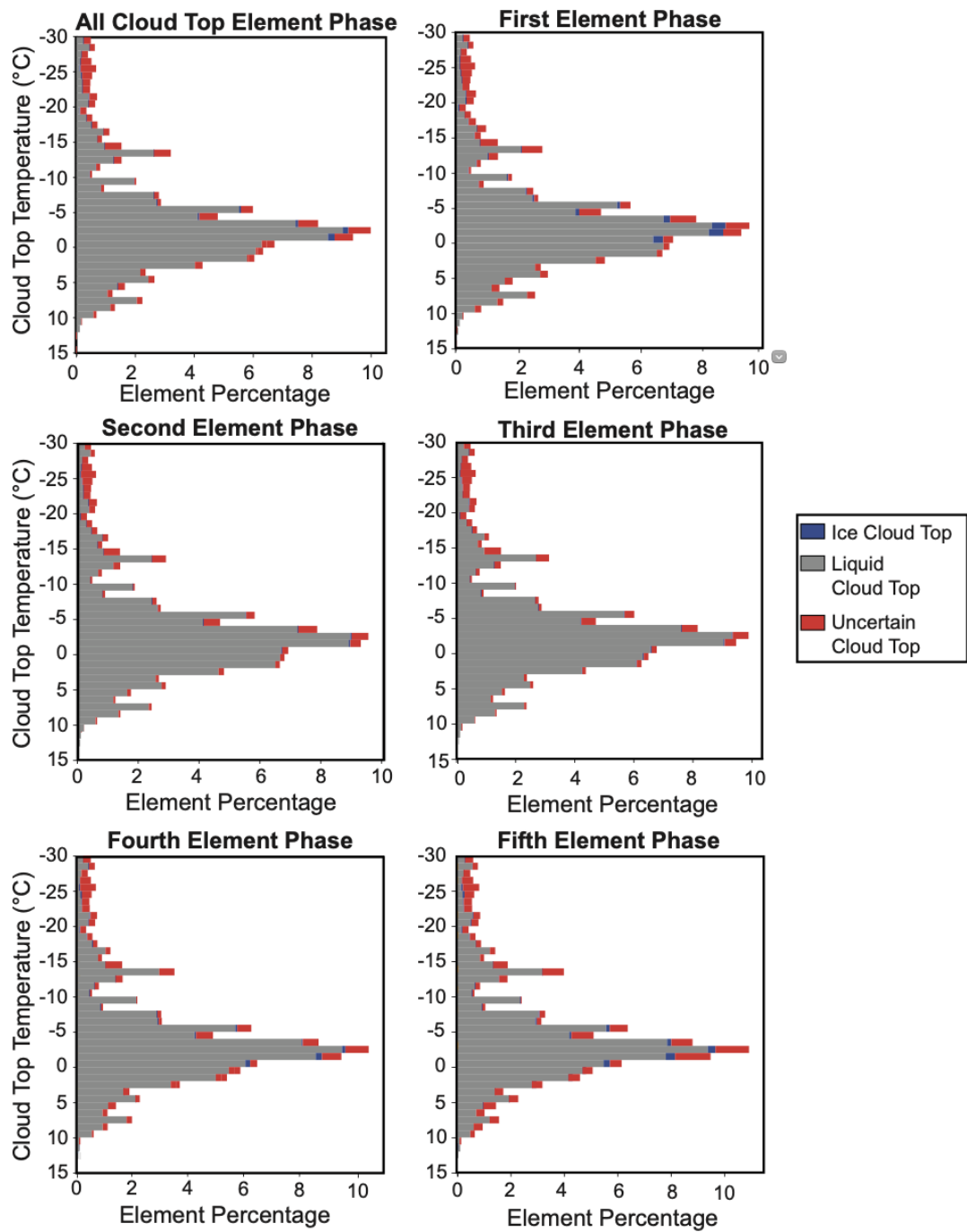


Fig. 18: Normalized percentage of phase detected in each of the five volume elements making up the cloud top, with 1 closest to cloud top and 5 at the base of the cloud top layer (See also Table 4).

922



923

924 Fig. 19: Cloud top phase as a function of CTT and depth within the cloud top layer (see also Table  
925 5).  
926

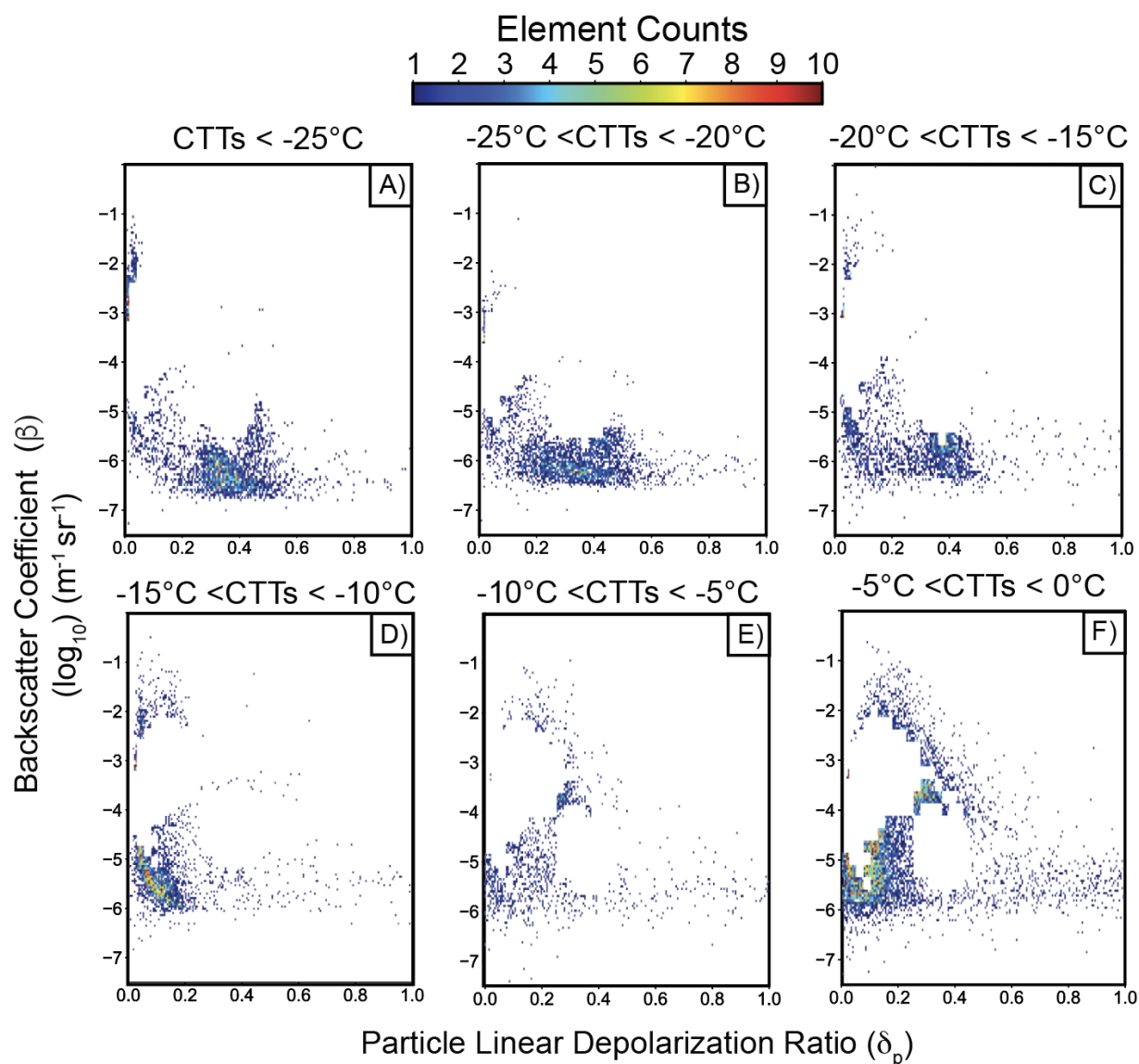
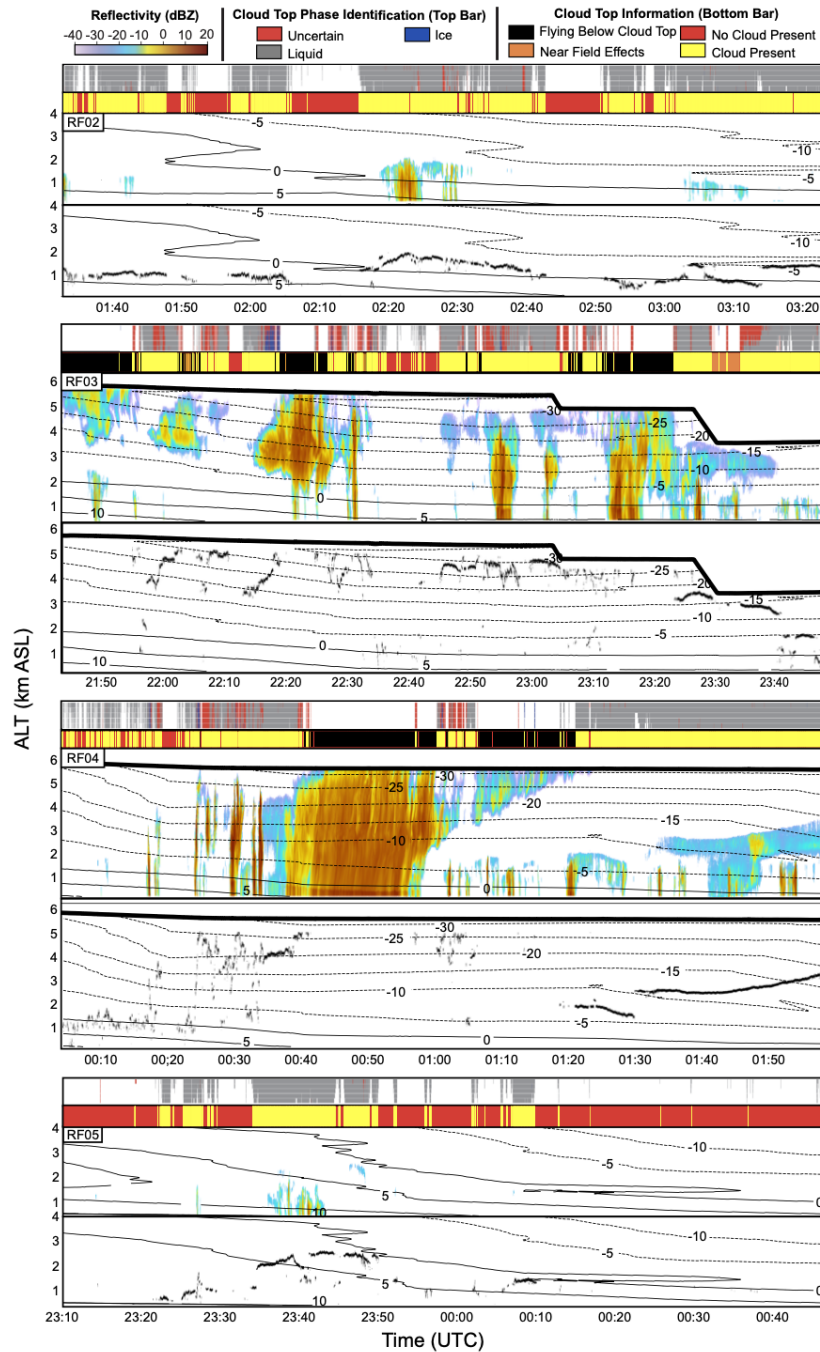


Fig. 20: Uncertain cloud top elements when reflectivity was above the noise threshold.



929

930 Fig. A1: Data from RF02, RF03, RF04 and RF05: Top panels for each flight:  $Z_e$  and Temperature  
 931 ( $^{\circ}\text{C}$ ); Bottom panels: Lidar detected cloud top for the top five cloud top elements. The lower bar  
 932 above each flight panel represents cloud top detection: red: no cloud present, yellow: cloud top  
 933 detected, orange: cloud top influenced by near field effects close to aircraft, black: aircraft in cloud.  
 934 The top bar represents cloud top phase: gray: liquid, blue: ice, red: uncertain.

935

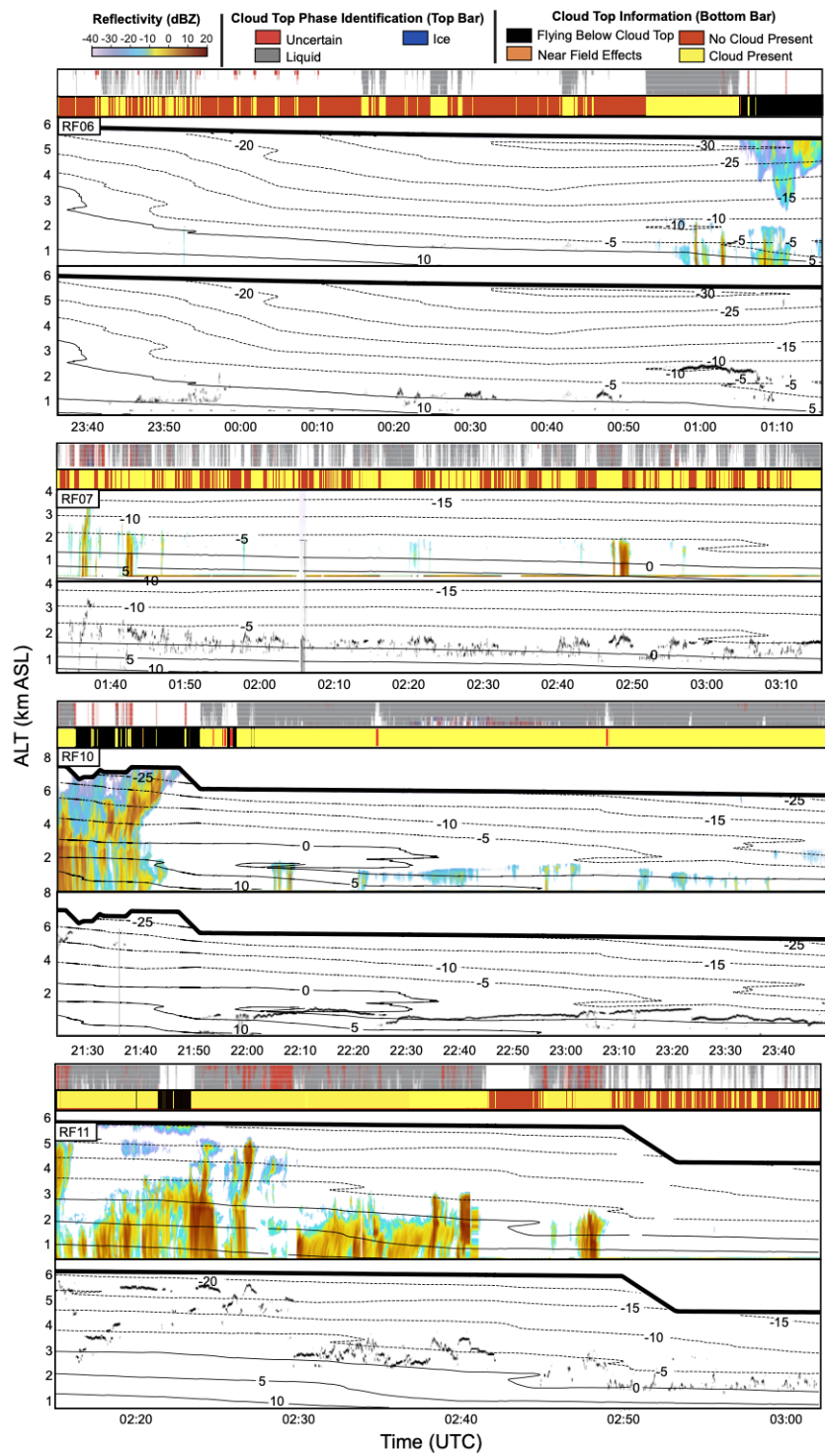


Fig. A2: Same as Fig. A1 except for research RF06, RF07, RF10, and RF11.



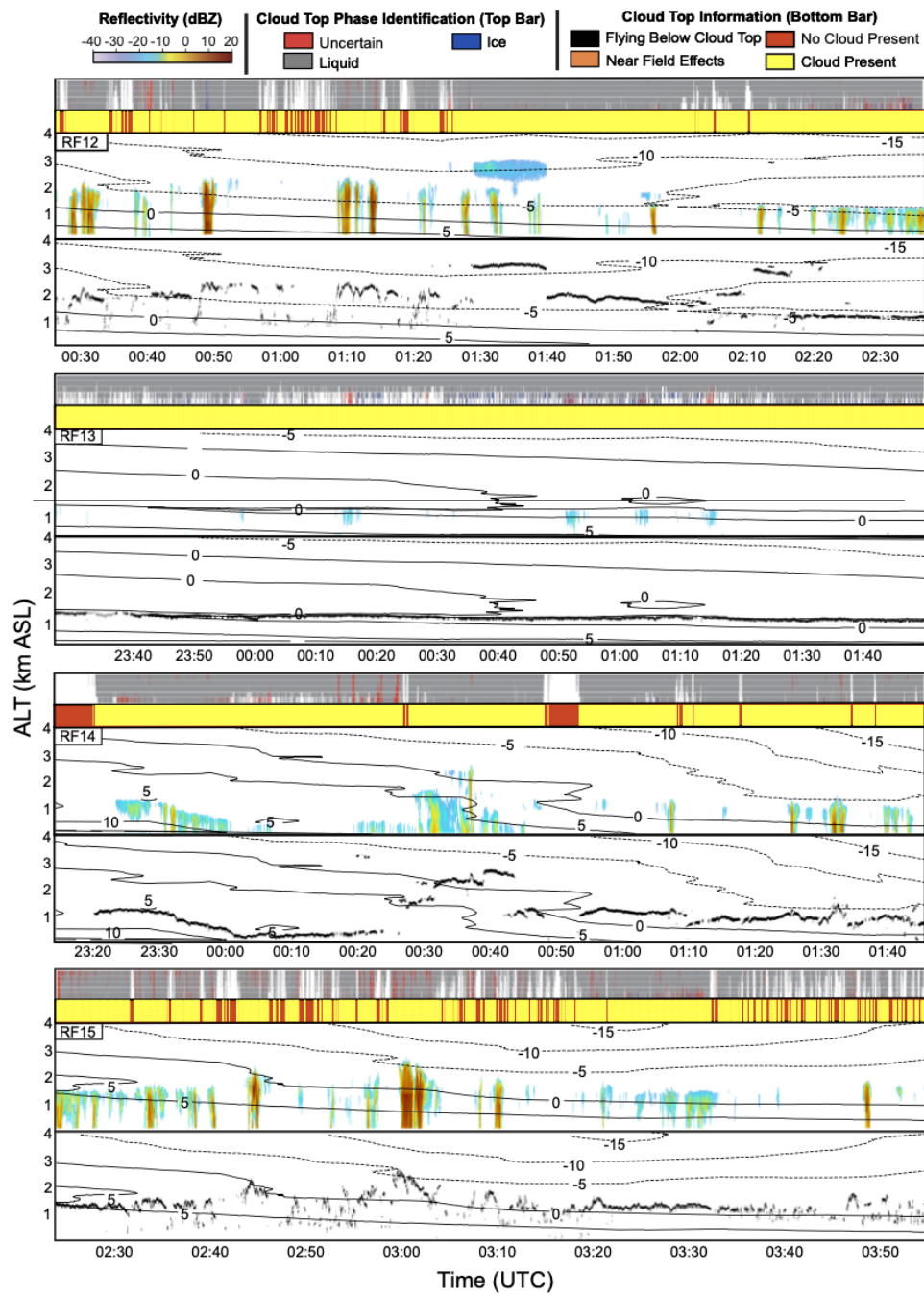


Fig. A3: Same as Fig. A1 except for RF12, RF13, RF14, RF15.